Pure Appl. Geophys. 173 (2016), 3999–4037

DOI 10.1007/s00024-016-1315-y

Pure and Applied Geophysics

Tsunami hazard assessment in the Hudson River Estuary based on dynamic tsunami–tide simulations

Michael Shelby,[1] Stéphan T. Grilli,[1] and Annette R. Grilli[1]

Abstract—This work is part of a tsunami inundation mapping activity carried out along the US East Coast since 2010, under the auspice of the National Tsunami Hazard Mitigation program (NTHMP). The US East Coast features two main estuaries with significant tidal forcing, which are bordered by numerous critical facilities (power plants, major harbors,...) as well as densely built low-level areas: Chesapeake Bay and the Hudson River Estuary (HRE). HRE is the object of this work, with specific focus on assessing tsunami hazard in Manhattan, the Hudson and East River areas. In the NTHMP work, inundation maps are computed as envelopes of maximum surface elevation along the coast and inland, by simulating the impact of selected probable maximum tsunamis (PMT) in the Atlantic ocean margin and basin. At present, such simulations assume a static reference level near shore equal to the local mean high water (MHW) level. Here, instead we simulate maximum inundation in the HRE resulting from dynamic interactions between the incident PMTs and a tide, which is calibrated to achieve MHW at its maximum level. To identify conditions leading to maximum tsunami inundation, each PMT is simulated for four different phases of the tide and results are compared to those obtained for a static reference level. We first separately simulate the tide and the three PMTs that were found to be most significant for the HRE. These are caused by: (1) a flank collapse of the Cumbre Vieja Volcano (CVV) in the Canary Islands (with a 80 km^3 volume representing the most likely extreme scenario); (2) an M9 coseismic source in the Puerto Rico Trench (PRT); and (3) a large submarine mass failure (SMF) in the Hudson River canyon of parameters similar to the 165 km^3 historical Currituck slide, which is used as a local proxy for the maximum possible SMF. Simulations are performed with the nonlinear and dispersive long wave model FUNWAVE-TVD, in a series of nested grids of increasing resolution towards the coast, by one-way coupling. Four levels of nested grids are used, from a 1 arc-min spherical coordinate grid in the deep ocean down to a 39-m Cartesian grid in the HRE. Bottom friction coefficients in the finer grids are calibrated for the tide to achieve the local spatially averaged MHW level at high tide in the HRE. Combined tsunami–tide simulations are then performed for four phases of the tide corresponding to each tsunami arriving at Sandy Hook (NJ): 1.5 h ahead, concurrent with, 1.5 h after, and 3 h after the local high tide. These simulations are forced along the offshore boundary of the third-level grid by linearly superposing time series of surface elevation and horizontal currents of the calibrated tide and each tsunami wave train; this is done in deep enough water for a linear superposition to be accurate. Combined tsunami–tide simulations are then performed with FUNWAVE-TVD in this and the finest nested grids. Results show that, for the 3 PMTs, depending on the tide phase, the dynamic simulations lead to no or to a slightly increased inundation in the HRE (by up to 0.15 m depending on location), and to larger currents than for the simulations over a static level; the CRT SMF proxy tsunami is the PMT leading to maximum inundation in the HRE. For all tide phases, nonlinear interactions between tide and tsunami currents modify the elevation, current, and celerity of tsunami wave trains, mostly in the shallower water areas of the HRE where bottom friction dominates, as compared to a linear superposition of wave elevations and currents. We note that, while dynamic simulations predict a slight increase in inundation, this increase may be on the same order as, or even less than sources of uncertainty in the modeling of tsunami sources, such as their initial water elevation, and in bottom friction and bathymetry used in tsunami grids. Nevertheless, results in this paper provide insight into the magnitude and spatial variability of tsunami propagation and impact in the complex inland waterways surrounding New York City, and of their modification by dynamic tidal effects. We conclude that changes in inundation resulting from the inclusion of a dynamic tide in the specific case of the HRE, although of scientific interest, are not significant for tsunami hazard assessment and that the standard approach of specifying a static reference level equal to MHW is conservative. However, in other estuaries with similarly complex bathymetry/topography and stronger tidal currents, a simplified static approach might not be appropriate.

1. Introduction

Tides and tsunamis are both long waves, whose propagation can accurately be modeled by a long wave theory (Dean and Dalrymple 1991), such as linear Stokes theory in deep water or Saint Venant (a.k.a., nonlinear shallow water equations; NSW) or Boussinesq equations in shallow water, depending on the relative magnitude of nonlinearity and dispersive effects. In deep water, tsunamis are not significantly

Electronic supplementary material The online version of this article (doi:10.1007/s00024-016-1315-y) contains supplementary material, which is available to authorized users.

[1] Department of Ocean Engineering, University of Rhode Island, Narragansett, RI 02882, USA. E-mail: michaelshelby@uri.edu; grilli@oce.uri.edu; agrilli@egr.uri.edu

affected by tides, because both the tidal range is small with respect to depth and tide-induced currents are very weak; hence, tsunami phase speed and shoaling are not significantly affected by the small change in water depth caused by tides. This also applies to shallow coastal water areas that have a simple bathymetry and a fairly straight coastline, as is the case for most of the ocean-exposed US east coast (USEC), from Florida to Massachusetts. There, while tide-induced currents may become larger and tidal range more significant as compared to the local depth, dynamic tidal effects are still small as compared to those in tsunamis, and tsunami inundation and runup can be accurately assessed by modeling tsunami propagation over a high static water level [typically the 10 % exceedance tide or the mean high water (MHW) level]. This was for instance the approach followed for performing tsunami inundation mapping in Ocean City, MD due to tsunamis caused by submarine mass failures (SMF) along the upper USEC (Grilli *et al.* 2015b).

When assuming a static increase of the mean water level (MWL) in model simulations, both tsunami phase speed and elevation will be affected by the increased depth, yielding larger inundation further onshore. However, in coastal regions where tidal range is large and/or bathymetry is complex (e.g., creating funneling effects), tide-induced currents may become larger and significantly vary in space, leading to potentially stronger and more dynamic tsunami–tide interactions. In such cases, earlier work (e.g., Tolkova 2013) indicates that one needs to more carefully and accurately model tsunami–tide interactions to achieve a conservative coastal hazard assessment. This requires, in particular, evaluating whether nonlinear and dynamic interactions between tide and tsunami currents and elevations may lead to more hazardous conditions than with the standard maximum static level approach. Along the USEC, significant tsunami–tide interactions could occur around the mouth of, and within a few large and complex estuaries, that are also highly populated areas having numerous critical infrastructures (such as major harbors and power plants), with prominent examples being New York, NY in the Hudson River estuary (HRE) and Norfolk, VA near the mouth of the James River estuary in the Chesapeake Bay, where the largest domestic US naval facility is located.

Since 2010, under the auspices of the US National Tsunami Hazard Mitigation Program (NTHMP; http://nthmp.tsunami.gov/index.html), the authors and colleagues from the University of Delaware have been developing tsunami inundation maps for the USEC (e.g., Tehranirad *et al.* 2014) by modeling coastal tsunami hazard from the Probable Maximum Tsunamis (PMTs) in the Atlantic Ocean basin. These PMTs

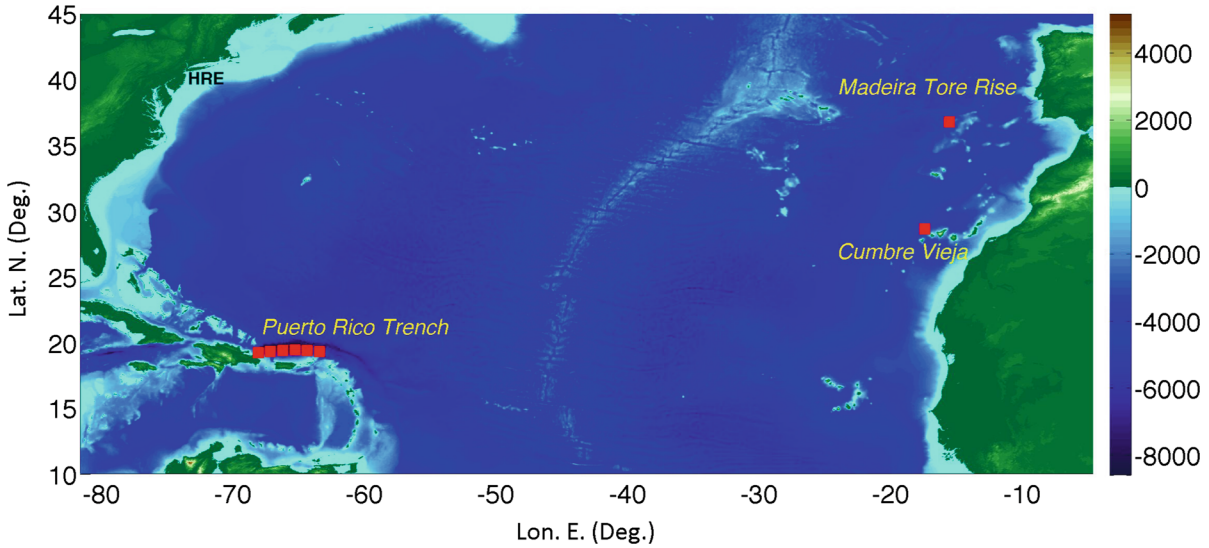

Figure 1
Footprint of the 1 arc-min resolution grid G4 in the Atlantic Ocean basin (Table 1), with marked locations of the three far-field PMT sources used in NTHMP work: MTR, CVV and PRT. The "HRE" label marks the location of the Hudson River Estuary mouth. Color scale is bathymetry (<0) and topography (>0) in meters, from ETOPO-1 data

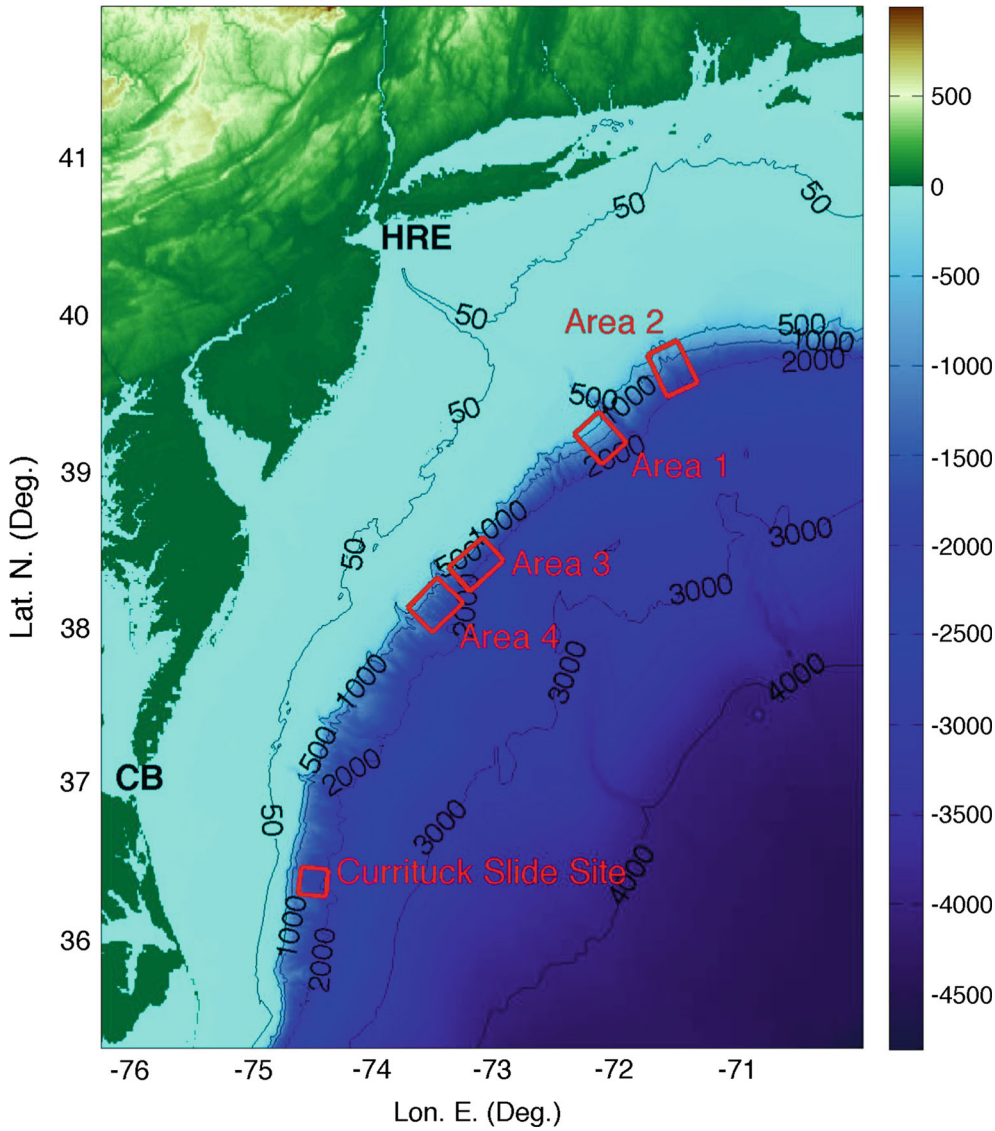

Figure 2
Zoom-in of Fig. 1 on upper US East Coast region encompassing two large estuaries modeled in the NTHMP tsunami–tide interaction work [Chesapeake Bay (CB) and Hudson River Estuaries (HRE)]; the figure covers the area where SMF tsunamis were simulated (from the Carolinas to Cape Cod). *Red boxes* mark locations of the historical Currituck slide site and of four areas (1–4) where large tsunamigenic SMF sources were sited (Grilli *et al.* 2009; 2015b) and parametrized as Currituck SMF proxies (Grilli *et al.* 2015b). Depth is in meters, in the color scale and bathymetric contours

included (Figs. 1 and 2; see also ten Brink *et al.* 2008, 2014; Grilli *et al.* 2015a): (1) near-field submarine mass failures (SMFs) on or near the continental shelf break, represented along the upper east coast by four large SMFs sited at selected locations, with the characteristics of the historical 165 km^3 Currituck (CRT) underwater landslide (Grilli *et al.* 2009, 2015b) (thus referred to as CRT SMF proxies; details will be provided later; Fig. 2); (2) an extreme hypothetical M9 seismic event occurring in the Puerto Rico Trench (PRT) (Grilli *et al.* 2010; Grilli and Grilli 2013b); (3) a repeat of the historical 1755 M9 earthquake occurring in the Azores convergence zone (MTR; Madera Tore Rise; Barkan *et al.* 2009; Grilli and Grilli 2013a); (4) an extreme flank collapse (80 and 450 km^3 volume scenarios) of the Cumbre Vieja

Volcano (CVV) in the Canary Islands (Ward and Day 2001; Abadie *et al.* 2012; Tehranirad *et al.* 2015). To develop tsunami inundation maps, simulations were performed using the fully nonlinear and dispersive model FUNWAVE-TVD (Shi *et al.* 2012; Kirby *et al.* 2013), by one-way coupling, in a series of coarse-to-finer nested grids. According to the standard methodology, in these simulations, the reference level in the coastal grids was set to a high tide value [such as the mean high water (MHW) level]. Hence, potential dynamic interactions between tide- and tsunami-induced flows were neglected.

It should be noted that in this past work Abadie *et al.* (2012) and Tehranirad *et al.* (2015) simulated two flank collapse scenarios for CVV, one with a 450 km^3 volume and geometry similar to Ward and Day's (2001) original scenario and one, deemed the most probable extreme scenario based on a slope stability analysis, with a 80 km^3 volume. In the tsunami hazard assessment work done for NTHMP, considering that the 450 km^3 CVV scenario is believed to have a return period of more than 100,000 years, it was decided to use the smaller, but likelier, 80 km^3 scenario, since its return period may be closer to that of the other extreme tsunami scenarios considered in the inundation mapping study (PRT, MTR, CRT), which have return periods on the order of hundreds to a few thousand years. Consistent with this rationale, the 80 km^3 CVV scenario was also used in the present tsunami–tide interaction study, which was conducted as part of NTHMP work. In their detailed modeling and comparison of the far-field impact of both CVV sources on the US East coast, Tehranirad *et al.* (2015) showed that for the 450 km^3 scenario very large incident waves, over 10–25 m high, were simulated off of the upper East Coast shelf (on the order of those also found by Ward and Day), but then bottom friction on the shelf reduced wave elevations significantly and the coastal inundation was predicted to be on the order of 3–6 m along the coast. They showed that, for the 80 km^3 scenario, the coastal inundation along the USEC was approximately reduced by a factor of 3, to 1–2 m. Ward and Day (2001) had predicted a much larger coastal impact along the USEC for their extreme CVV scenario, but their modeling approach had important differences with that of Abadie *et al.* (2012) and Tehranirad *et al.* (2015). Abadie et al simulated the subaerial landslide resulting from the CVV flank collapse with a multi-fluid 3D full Navier Stokes model, and then propagated the tsunami with the fully nonlinear and dispersive long wave model FUNWAVE, with the inclusion of dissipation from bottom friction and breaking. By contrast, Ward and Day (2001) used a simplified slide model and a propagation model based on linear theory without dissipation; the latter model led to significantly overestimating coastal wave impact.

To date, interactions between tide and tsunami waves have only rarely been studied. Kowalik *et al.* (2006) first hypothesized that, for strong tidal flows, significant effects due to tsunami–tide interactions should be observed in the tidal and tsunami currents. Kowalik and Proshutinsky (2010) then modeled tsunami–tide interactions in Cook Inlet (Alaska), which has one of the largest tidal ranges in North America. They showed that results significantly differed from a simple linear superposition of separate simulations of tide and tsunami and that maximum elevations depended on the tide amplitude and phase; with tsunami being intensified or damped, depending on mean basin depth, which is regulated by tides. They concluded that, in their simulations, the main effects of the tide were to change water depth, thus affecting tsunami phase speed, propagation, amplification, and dissipation by bottom friction. These, however, were site-specific conclusions and tsunami–tide interactions effects cannot a priori be predicted without performing dynamical simulations combining tide and tsunami forcing. Zhang *et al.* (2011) performed high-resolution simulations of the impact of the 1964 Prince William Sound tsunami on the US Pacific Northwest coast, with and without dynamic tide effects, and evaluated tidal influence on wave elevation, velocity, and inundation. As could be expected, results showed that the tide had minimal effects near the open coast, but significantly affected both wave run-up and inundation near the mouth of and within estuaries and rivers. On this basis, they concluded that dynamic tsunami–tide interactions should be considered in estuaries, as these could account for 50 % of the observed run-up and up to 100 % of the inundation in some cases. To better understand the observed 100 km upstream

propagation of the Tohoku 2011 tsunami in the Columbia River (Oregon), Yeh *et al.* (2012) and Tolkova (2013) modeled tsunami–tide interactions. Tolkova found that tsunami waves propagated further on a rising tide in the lower portion of the river; however, upstream the tsunami propagated further at the maximum high tide; results also showed a potential amplification of tsunami waves directly after high tide. Tolkova concluded that the interaction of the two long waves is completely dependent on the specific environment in which the interaction occurs, which justifies performing site-specific studies. More recently, performing similar studies based on data from a river in Japan, Tolkova *et al.* (2015) showed that the Tohoku 2011 tsunami had caused increased surface elevations in the river by hindering drainage; this translated into increased tsunami inundation during tidal ebb. In the same geographic area, Nakada *et al.* (2015) performed high-resolution simulations of tsunami–tide interactions for the propagation in Osaka Bay of a large tsunami generated in the Nankai Trough. To quantify tide effects they run many cases in which tsunami propagation started every hour, through two tidal cycles. They concluded that strong flood or ebb tidal currents modulated tsunami arrival by a few minutes and led to increased elevation in many situations, particularly during strong ebb flows, as compared to a static computation.

As part of the NTHMP USEC work, Tajalli-Bakhsh *et al.* (2014) modeled dynamic tsunami–tide interactions in Chesapeake Bay, with particular focus on assessing tsunami hazard in the James River, which is most affected by tidal currents and has the Norfolk Naval facility at its mouth and a nuclear power plant upstream. They considered the M2 tidal component in the Bay and combined it, for different phases, with the two worst case scenario PMTs identified for this area, i.e., tsunamis generated by an extreme CVV flank collapse and the historical Currituck underwater slide, whose site is located near the mouth of the Bay (Geist *et al.* 2009; Grilli *et al.* 2015b) (Fig. 2). While results showed clear nonlinear tsunami–tide interactions, affecting both tsunami elevation and propagation speed in the river, maximum tsunami inundation did not exceed that computed over a static reference level equal to the maximum elevation of the dynamic tide at the river mouth (here, the 10 % exceedance maximum tide level).

Earlier studies summarized above all concluded that tsunami–tide interaction effects are largely site specific. In the Chesapeake Bay, one of two large estuaries located along the USEC considered in NTHMP work, Tajalli-Bakhsh *et al.* (2014) concluded that this more advanced modeling approach was not necessary for proper tsunami hazard assessment. Here, following a similar methodology, we simulate the combined effects of tides of various phases on the evolution of tsunami waves in the HRE (Fig. 1), to compute maximum inundation elevation and limits. [Note that, for simplicity we use HRE to refer to the New York Bay tidal system, including the Hudson River estuary and East River.] Based on the earlier work on Atlantic tsunami source modeling summarized above (Grilli *et al.* 2015a), the three PMTs selected to perform inundation mapping in the HRE area for NTHMP, representing the most likely extreme events that can potentially affect this region of the USEC, are: (1) a Currituck SMF proxy sited on the continental slope off of the Hudson River canyon (Grilli *et al.* 2015b) (see "Study Area 1" in Fig. 2); (2) a 80 km^3 flank collapse of the Cumbre Vieja Volcano in the Canary Islands (Abadie *et al.* 2012; Tehranirad *et al.* 2015); (3) a magnitude 9.0 earthquake in the Puerto Rico Trench (Grilli *et al.* 2010; Grilli and Grilli 2013b). The HRE has particularly strong tidal currents (1–2 kts, i.e., nearly twice the speed of currents in Chesapeake Bay) and also has been identified as one of the highest risk areas along the USEC for flooding caused by a tsunami resulting from a submarine mass failure (SMF) occurring in the Hudson River Canyon (Grilli *et al.* 2009); this led Grilli *et al.* (2015b) to define a CRT SMF proxy sources in the HRE canyon area (Fig. 2).

Besides being part of the NTHMP work scope of performing conservative tsunami hazard assessment for all US coastal areas, the HRE is another complex tidal system to assess the importance of nonlinear exchanges of energy between tide and tsunami, similar to the work done by Tolkova (2013) in the Columbia River. There, Tolkova found that tsunami signals propagating with the low tide were gradually

damped out, while those traveling with the high tide were preserved or amplified. This was most apparent at the farthest upstream station for which data for the Tohoku 2011 tsunami were collected. Similar phenomena were observed by Tajalli-Bakhsh *et al.* (2014) for tsunamis propagating up the James River, although as indicated this did not lead to higher inundation than for a static tide level. If the Hudson River results are consistent with Tolkova's findings, differences between static and dynamic tsunami–tide simulations should be larger at upstream locations when propagating over a high tide.

In the following, to assess dynamic tsunami–tide interactions in the HRE we perform two sets of simulations. First, for each PMT, we simulate tsunami propagation into the HRE assuming a static tide level equal to the local MHW level. Then we perform joint tsunami–tide simulations for four phases of tidal forcing achieving a maximum level identical to MHW in the HRE. The methodology for performing combined tsunami–tide simulations, which is similar to that used by Tajalli-Bakhsh *et al.* (2014), is detailed in the next section. We then briefly detail the computational model and present grid setup. We finally report in detail and compare results of the two sets of simulations. Note that the choice of MHW for the static and maximum tide levels is consistent with the standard approach in tsunami inundation mapping done for NTHMP. Tajalli-Bakhsh *et al.* (2014) used the slightly higher 10 % exceedance tide level in Chesapeake Bay for both static and dynamic simulations, because tsunami hazard was also assessed at a nuclear power plant in the James River, which required to be slightly more conservative.

2. *Modeling methodology and model grids*

2.1. *Models and modeling methodology*

All simulations, both tide and tsunami, alone or combined, are performed using the fully nonlinear and dispersive Boussinesq model FUNWAVE (Wei *et al.* 1995; Grilli *et al.* 2007, 2010; Ioualalen *et al.* 2007), in its most recent Cartesian (Shi *et al.* 2012) and spherical (Kirby *et al.* 2013) implementations referred to as FUNWAVE-TVD (the spherical implementation including Coriolis effects). FUNWAVE-TVD is fully parallelized for an efficient solution on shared memory clusters and uses an efficient total variation diminishing (TVD) algorithm to follow breaking wave fronts in shallow water. The model has a quadratic bottom friction term controlled by a Manning friction coefficient n and, unlike the original FUNWAVE, it models dissipation in breaking waves by turning off dispersive terms in areas where breaking is detected based on a breaking index criterion (see details in Shi *et al.* 2012). While FUNWAVE-TVD's Cartesian implementation is fully nonlinear, its spherical implementation is only weakly nonlinear; hence, it is only used in areas where tsunami elevation over local depth is in the order of 10 % or less. Therefore, in tsunami simulations, spherical grids are typically fairly coarse and used to model large ocean areas in relatively deeper waters, whereas Cartesian grids have a higher resolution and are used to model coastal tsunami impact. This approach was successfully used to model the Tohoku 2011 tsunami in both the near and far field (Grilli *et al.* 2013; Kirby *et al.* 2013). Both implementations of FUNWAVE-TVD have been fully validated against standard benchmarks as part of the NTHMP work (Tehranirad et al. 2011; Shi *et al.* 2012b).

Simulations with FUNWAVE-TVD are performed in several levels of overlapping nested grids, using a one-way coupling methodology. This works by computing time series of free surface elevations and currents in a coarser grid level, for a large number of numerical gages (stations) defined along the boundary of the finer grid level. Computations in the finer nested grid level are then performed using these time series as boundary conditions. With this approach, reflected waves propagating from inside the area covered by each finer grid are included in the time series computed in the coarser grids along the finer grid boundaries, thus satisfying an open boundary condition. For far-field tsunami simulations, to reduce reflection in the first coarsest grid level (here the 1 arc-min Atlantic Ocean basin grid G4 used to compute the transoceanic propagation of the CVV and PRT sources; Fig. 1), 200-km-thick sponge (absorbing) layers are specified along all the open boundaries. For the near-field CRT

SMF proxy tsunami, the first-level grid is initialized with the surface elevation and horizontal velocity computed using the three-dimensional model NHWAVE (Ma *et al.* 2012) (see details in Grilli *et al.* 2015b).

For the dynamic tsunami–tide simulations, we follow the methodology that was first applied by Tajalli-Bakhsh *et al.* (2014) in the Chesapeake Bay estuary, i.e., we:

1. Simulate the propagation of the selected PMTs from their source, in a series of nested grids, to a moderate resolution regional grid (here the 154-m resolution grid G2; Fig. 3; Table 1) encompassing the HRE (Fig. 3).
2. Simulate and calibrate the tide for its maximum elevation to reach the local MHW level in the HRE area, based on reference results available at a series of NOAA tide gages in the estuary; bottom friction values are adjusted in the model, if necessary, to achieve a better agreement (calibration phase). The uncalibrated tidal forcing (both surface elevation and current) is obtained from a separate global model (detailed later) and specified along the boundary of the medium-size regional grid encompassing the HRE (here the 616-m resolution grid G3b; Fig. 3; Table 1).
3. Then jointly simulate tide and tsunami, by linearly superimposing incoming tsunami wave elevations and velocities with tidal forcing, along the

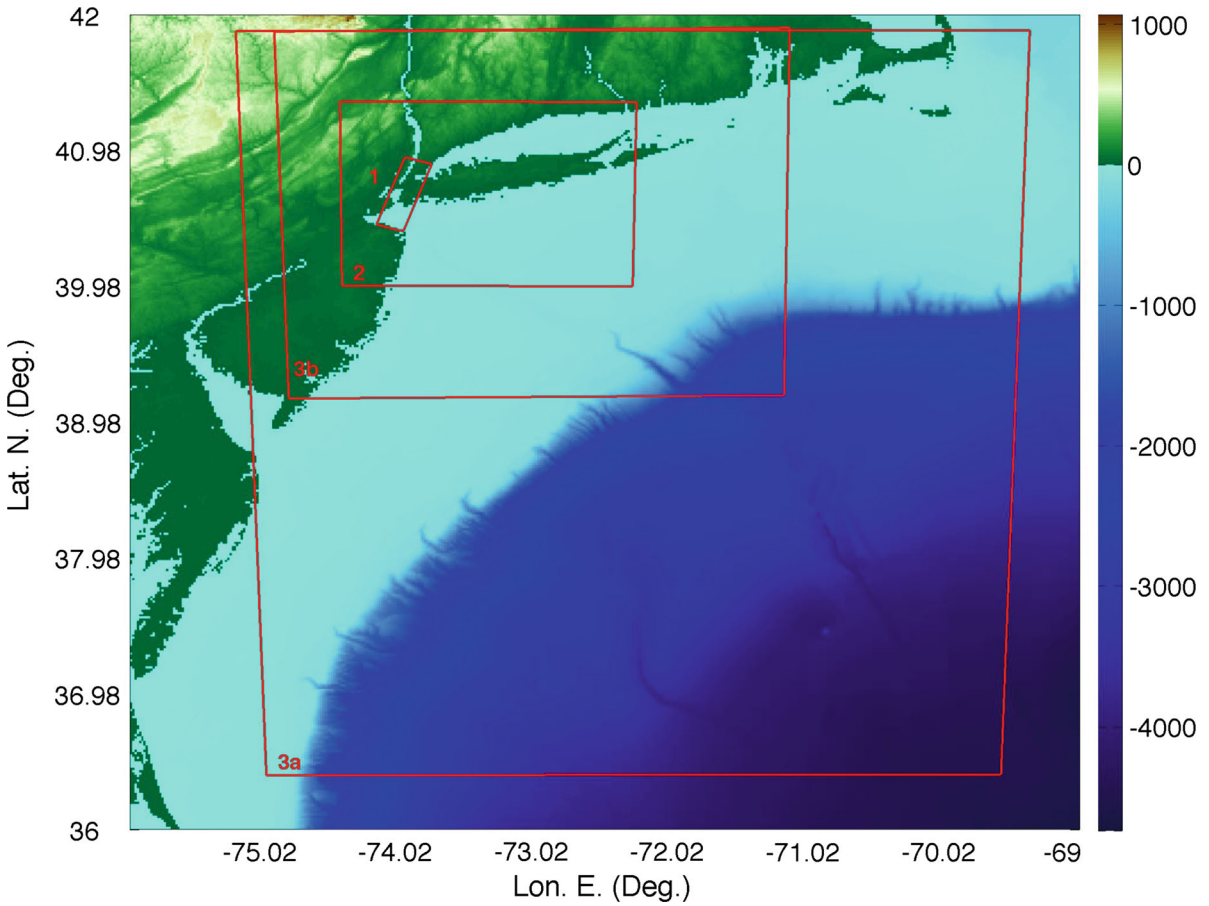

Figure 3

Regional and near-shore computational grids used in tide, tsunami-only, and tsunami–tide simulations with FUNWAVE-TVD (labeled *red boxes* correspond to grids defined in Table 1). Tide-only simulations are initiated in grid 3b, and then nested into grids 2 and 1. After being initiated in the 1 arc-min grid G4 (Fig. 1), simulations of far-field tsunami sources (CVV, PRT) are pursued in nested grids G3b, G2 and G1. Simulations of the near-field CRT proxy SMF tsunamis are performed in grids G3a, G2, and G1. All tsunami–tide simulations are initiated in grid G2 and then pursued in grid G1. Color scale is bathymetry (<0) and topography (>0) in meters

Table 1

Parameters of computational grids used in FUNWAVE-TVD model (Figs. 1, 3) to compute the propagation of far-field (G4, G3b, G2, G1; CVV and PRT) and near-field (G3b, G2, G1; CRT SMF proxy 1; Fig. 2) tsunami sources, and tides (G2, G1). "Res." is resolution of spherical (S) or Cartesian (C) type grids and N_x and N_y indicate the number of grid cells in each direction

Grid/ type	SW Lat. (*N* deg.)	NE Lat. (*N* deg.)	SW Lon. (*W* deg.)	NE Lon. (*W* deg.)	Res.	N_x	N_y
G4/S	10	45	82	5	1 min	4620	2100
G3a/C	36.396	41.885	74.994	69.25	616 m	788	990
G3b/C	39.171	41.904	74.829	71.138	616 m	512	489
G2/C	40.003	41.355	74.437	72.266	154 m	1188	980
G1/C	39.171	40.900	74.829	73.775	38.5 m	459	1504

offshore boundary of a computational grid selected with a depth large enough along its offshore boundary to justify such a linear superposition (here, grid G2).

4. Finally, simulate effects of tide phase on the three incident tsunamis by considering four different phases when peak tsunami and time-shifted tide signals are superimposed along the boundary of grid G2.

2.2. Grid bathymetric data

Besides their footprint, resolution, and type (spherical or Cartesian), each model grid requires a depth matrix that is developed by interpolating bathymetric and topographic data of resolution commensurate with that of the grid. The key parameters for each model grid are listed in Table 1 and their footprints are shown in Figs. 1 and 3. In earlier NTHMP work, bathymetry and topography for such grids was interpolated from the most accurate sources available, i.e., the 1 arc-min ETOPO-1 data in deeper water, 1 or 3 arc-s (30 or 90 m) NOAA Coastal Relief model data (NOAA-NGDC 2013) over the shelf, and 1/3 arc-s (10 m) NTHMP or Federal Emergency Management Agency (FEMA) Region II Digital Elevation Models (DEMs) wherever available (FEMA 2014).

In analyzing NOAA's detailed bathymetric data used for coastal hazard assessment in the HRE, we noted a paucity or even a lack of data in the vicinity of Manhattan Island. This region, however, is critical for considering tsunami effects in the Hudson River. Hence, in this region, near-shore bathymetry was obtained from FEMA, with a resolution of about 8 m [Fig. 4; FEMA (2014)]. Thus, grid G4's depth matrix is based on ETOPO-1 data, while that of grids G3a,b is based on ETOPO-1 and 90 m DEM data. All of grid G1 and part of grid G2's depth matrix are based on FEMA's 8 m DEM and parts of Grid G2 that are not included in this high-resolution data were completed using NOAA's 90 m DEM. Figure 5 shows the resulting (interpolated) bathymetry and topography for grids G1 and G2. The vertical datum is referenced in all grids to NAVD88. Note that grid G1 is oriented at 18° clockwise from north (Fig. 3) to allow for a more efficient use of grid points, which significantly reduces the model computational time.

2.3. Fresh water discharge

Finally, the fresh water discharge from the Hudson River was estimated at 600 m^3/s (USGS 2010), compared to a maximum tidal volume flux through the mouth of the Hudson River during an MHW tide at Manhattan Island of over 6000 m^3/s. The latter is based on currents and surface elevations computed at the mouth of the Hudson River using FUNWAVE-TVD, for tide-only simulations (see details in next section). The transect where the tidal flux calculation is made is marked in Fig. 7. Because the river discharge is small as compared to the tidal flux and to isolate tidal effects, river discharge and related current are neglected in this study.

3. Tide-only simulations

Tide propagation is first simulated in the HRE to identify and calibrate conditions causing a maximum

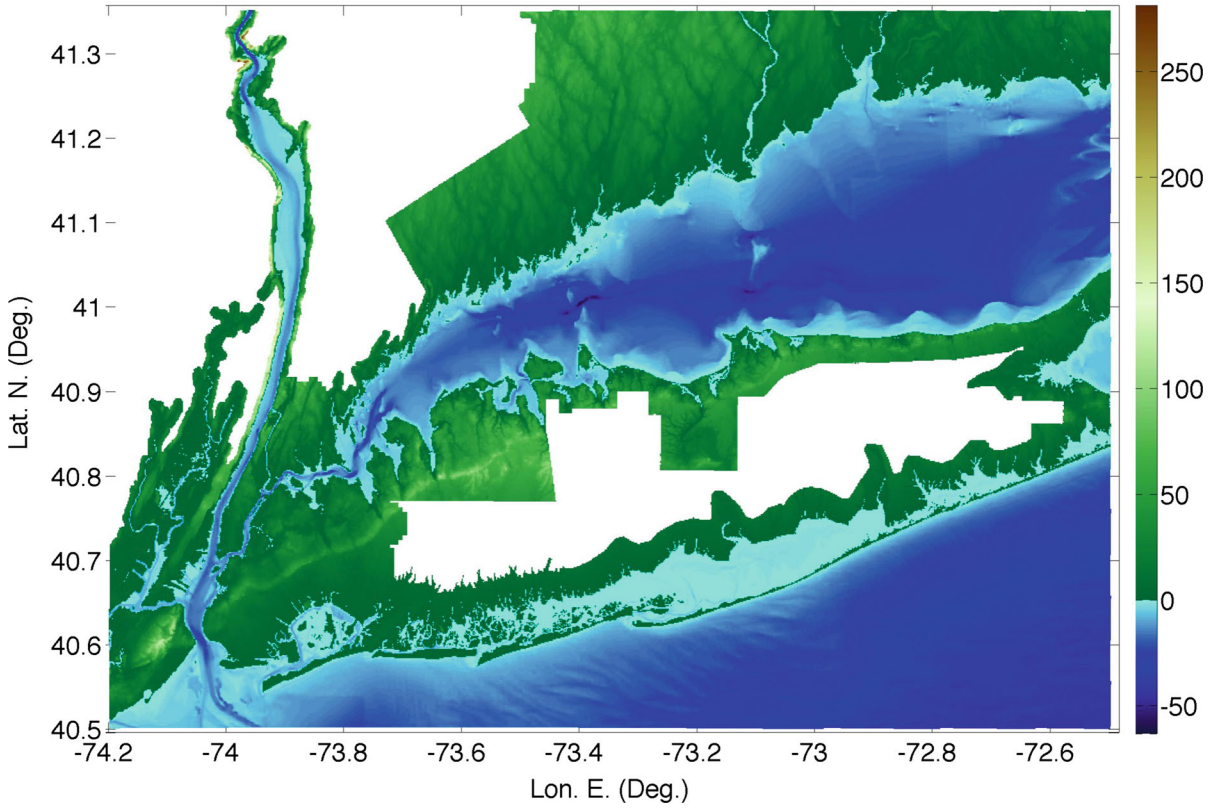

Figure 4
High-resolution bathymetric/topographic data in HRE's area of interest, from FEMA's 8 m DEM (FEMA 2014), used to define the finest resolution grid G1's depth matrix. These data were combined with the 90 m NOAA DEM data to define grid G2's depth matrix (Table 1). Color scale is bathymetry (<0) and topography (>0) in meters, referenced to the NAVD88 vertical datum

tidal elevation equal to the local MHW level at selected NOAA tide gages. A 24-h time interval was first identified, between 7:00 am on 13 July 2015 and 7:00 am on 14 July 2015, during which maximum tidal elevations nearly reached MHW at the tide gages (NOAA's tide gage data listed in Table 2 indicates that MHW level varies between 0.57 and 1.19 m NAVD88 in the HRE). Tide propagation was then simulated during this time interval with FUNWAVE-TVD, in the 616-m resolution grid G3b, based on boundary and initial conditions (surface elevation and horizontal velocity) obtained from a large-scale barotropic tide model: the "Oregon Tide Prediction Software" (OTPS). In the grid G3b simulations, tidal forcing was computed along the boundary of the 154-m resolution nested grid G2 (Fig. 3), in the form of time series of free surface elevations and currents at many control stations, following the one-way coupling method detailed before. This procedure was finally repeated for grid G1. Based on differences observed between modeled and reference surface elevations at 14 NOAA gages located within grid G1, simulations were repeated with modified bottom friction coefficients in grid G1, to achieve the best possible agreement.

OTPS' latest version TPXO8 predicts tidal elevations and currents along the USEC, in a 2 arc-min grid. Considering this is a fairly coarse grid, OTPS' results are more accurate offshore, in deeper water (Stammer *et al.* 2014). Accordingly, tide simulations with FUNWAVE were initiated in the larger, coarser resolution, domain G3b, whose boundary is mostly located in fairly deep water. Following Tajalli-Bakhsh et al.'s (2014) approach, boundary conditions were ramped up using a "tanh" function, from zero to the OTPS' model predictions, over nearly a half-

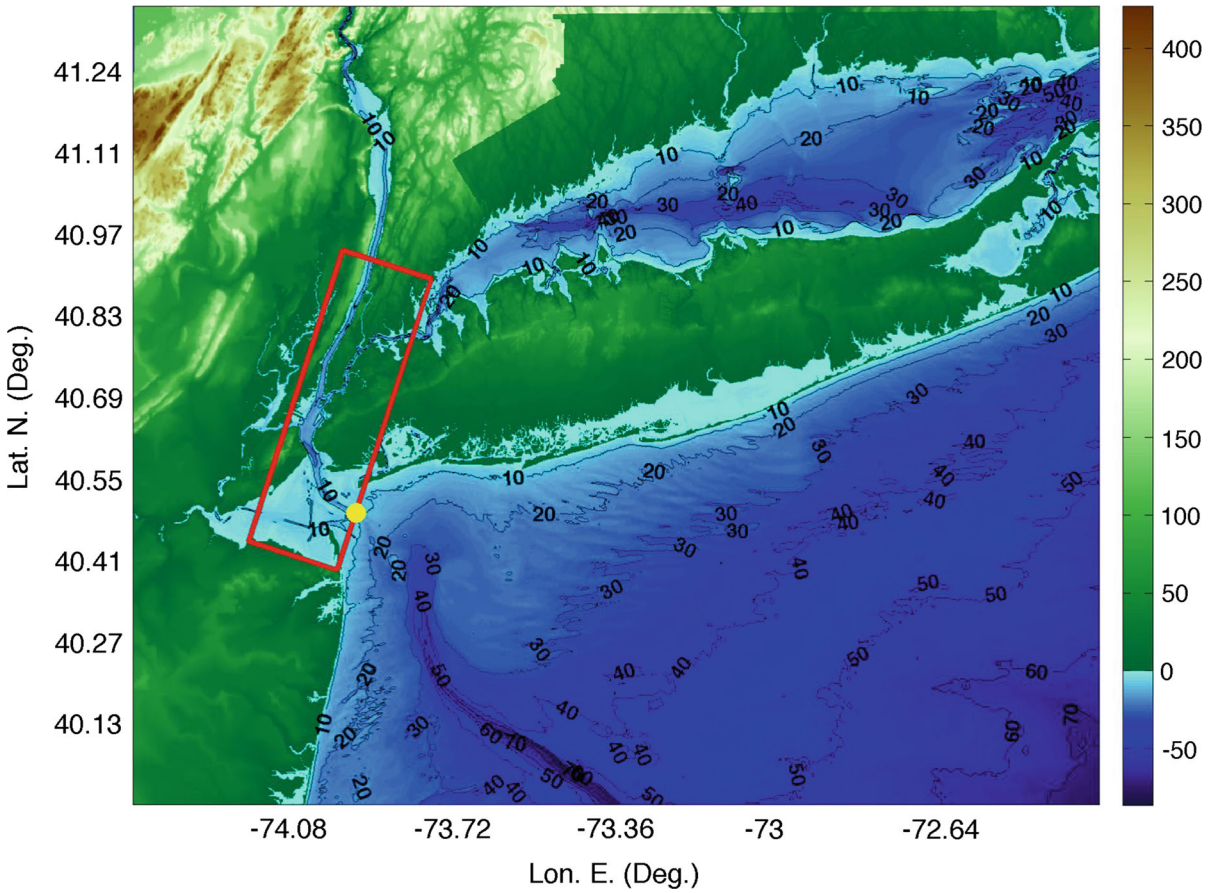

Figure 5
Interpolated bathymetry and topography used in grids G1 (*red box*) and G2 (footprint of the figure; Table 1), encompassing the HRE, where dynamic tsunami–tide simulations are performed and compared to simulations over a static tide level. Color scale and black contours are bathymetry (<0) and topography (>0) in meters, referenced to the NAVD88 vertical datum. Note the deep Hudson River canyon offshore of the HRE mouth. The *yellow bullet* marks the location of a numerical gage placed at the entrance to Lower Bay (−73.944 Lon. E., 40.501 Lat. N, local depth 16.9 m), where time series of surface elevations are computed in Fig. 13 for the three incident tsunamis

semidiurnal tidal cycle (6 h). Model results were allowed to stabilize for another 12 hours before being computed and specified along the boundary of grid G2, and so forth in grid G1. To validate and calibrate tide simulations, surface elevations were computed at the locations of twenty NOAA tide gages in the HRE area (Table 2; Fig. 6), which includes 2 actual tide gages, at Sandy Hook and Battery Point, and 18 virtual tide gages where corrections are made by NOAA with respect to the actual gages, based on a harmonic analysis. At some of these virtual gages, referred to as subordinate stations (numbered #2 to #7 and #13 to #16 in Fig. 6), only maximum and minimum tide levels and their time of occurrence are provided; at the other virtual stations, full time series are provided. Figure 6 shows that all 20 stations are located within grid G2, but only 14 stations are located within grid G1 (Fig. 7a). Numerical results obtained for the maximum surface elevation η_m during the second tidal cycle were compared to the reference maximum for each gage η_p, which we verified was close to the local MHW level for the selected time interval.

After this initial tide simulation, the Manning friction coefficient n was adjusted in grid G1 to improve the agreement between the modeled and known maximum elevations at NOAA's tide gages. By observing discrepancies at these stations (marked in Fig. 7a), n was adjusted to 0.015 in the Hudson and East Rivers, north of Battery Point, while a value

Table 2

Definition and location of NOAA tide gage stations marked in Fig. 6. The maximum water level elevation with respect to the NAVD88 datum is given at each station for the NOAA high-tide (MHW) prediction η_p, compared to surface elevation η_m modeled with FUNWAVE-TVD in the 154-m resolution grid G2 and 38.5-m resolution grid G1 (note, only 14 stations are located within this grid); the absolute $(\eta_m - \eta_p)$ and relative differences between these $((\eta_m - \eta_p)/\eta_p)$ are listed for each grid

Tide Gage Station				NOAA	Grid G2 (154 m)			Grid G1 (38.5 m)		
No.	Name	Lat. N. (Deg.)	Lon. E. (Deg.)	η_p (m)	η_m (m)	Absol. diff. (m)	Relat. diff. (%)	η_m (m)	Absol. diff. (m)	Relat. diff. (%)
#1	Sandy Hook	40.7003	−74.0135	0.71	0.78	0.07	9.42	0.73	0.02	3.24
#2	Atlantic Highlands	40.4183	−74.0200	0.72	0.78	0.06	8.58	0.74	0.02	2.56
#3	Waackaack	40.4483	−74.1433	0.72	0.82	0.11	15.25	0.78	0.07	9.37
#4	Princes Bay	40.5117	−74.2000	0.75	0.84	0.08	11.09	–	–	–
#5	Coney Island	40.5667	−73.9833	0.71	0.76	0.05	7.62	0.71	−0.00	−0.02
#6	Fort Hamilton	40.6083	−74.0350	0.73	0.80	0.07	9.14	0.71	−0.02	−3.39
#7	St. George	40.6433	−74.0733	0.66	0.78	0.11	17.19	0.72	0.05	7.79
#8	Gowanus Bay	40.6650	−74.0133	0.71	0.78	0.08	11.27	0.72	0.01	2.05
#9	Battery Point	40.4665	−74.0094	0.69	0.77	0.08	12.04	0.71	0.02	2.89
#10	Williamsburg Bridge	40.7117	−73.9683	0.59	0.72	0.13	22.73	0.69	0.10	17.44
#11	Horns Hook	40.7767	−73.9417	0.69	0.55	−0.14	−19.85	0.75	0.06	9.41
#12	Willets Point	40.7933	−73.7817	1.16	0.98	−0.18	−15.77	–	–	–
#13	Union City	40.7667	−74.0183	0.65	0.65	0.00	0.03	0.67	0.02	2.66
#14	Edgewater	40.8133	−73.9783	0.63	0.51	−0.12	−18.73	0.63	−0.01	−0.82
#15	Spuyten Duyvil	40.8783	−73.9250	0.56	0.36	−0.20	−35.52	0.58	0.01	2.18
#16	Riverdale	40.9033	−73.9167	0.58	0.33	−0.25	−42.93	0.58	−0.01	−0.91
#17	Glen Cove	40.8633	−73.6550	1.19	0.96	−0.23	−19.62	–	–	–
#18	Long Neck Point	41.0383	−73.4800	1.08	0.90	−0.18	−16.50	–	–	–
#19	Cedar Beach	40.9650	−73.0433	0.97	0.77	−0.20	−20.95	–	–	–
#20	Northsville	40.9817	−72.6450	0.81	0.62	−0.19	−22.86	–	–	–

$n = 0.025$ was used in the remainder of grid G1; this value was also used in grid G2. The corresponding friction coefficient, $C_d = gn^2/h^{1/3}$ is plotted in Fig. 7d for grid G1 (with g the gravitational acceleration and h, here, being the local depth with respect to NAVD88, i.e., not including surface elevation); C_d values are seen to vary between 0.001 and 0.005, i.e., they are both lower and higher than $C_d = 0.0025$, the standard value for coarse sand. The fairly straight Hudson River has a hard muddy bottom and a regular cross section, supporting the use of a lower n value. Since both tide and tsunami are long waves causing significant flow velocity near the bottom, it is reasonable to use the same bottom friction values in simulations of tsunami-only propagation into the HRE, as well as in tsunami–tide simulations.

Following the calibration of bottom friction, the resulting maximum surface elevations modeled at the NOAA tide gages, and their absolute and relative differences with NOAA's reference values at the 20 stations in grids G1 and G2 are listed in Table 2 for each station. Additionally, Fig. 8 shows a comparison of time series of surface elevations modeled at the stations with NOAA's reference data (either full time series or only extrema, whichever is available). The agreement between these appears visually quite good, and more so for results in the higher resolution grid G1, particularly at gages #5 to #11 and #13 to #16, which are located in the most important areas considered here: New York harbor, and the Hudson and East Rivers around Manhattan. Table 2 shows that the modeled maximum tide elevations in grid G1 are within 0.02 m of NOAA's reference data at 8 of these 11 stations (with a 2.2 % RMS for their relative difference); two stations (#7 and #11) have differences of 0.05 and 0.06 m and the largest difference (0.10 m) is observed at the Williamsburg Bridge station. For these 14 stations, the RMS of the relative difference between modeled and predicted results is 6.5 %. Hence, the overall agreement of model results with NOAA's reference data in grid G1 appears to be good, particularly in the area where we will analyze

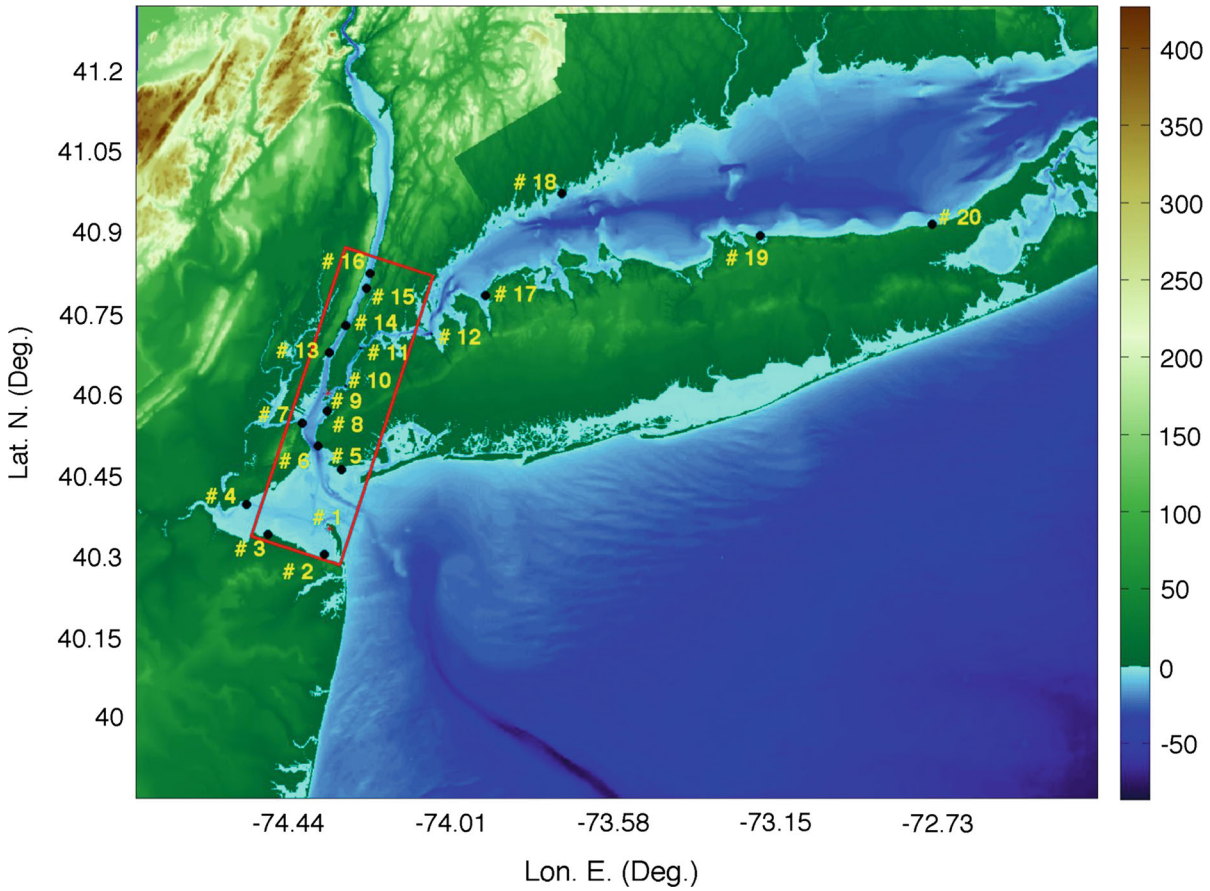

Figure 6
Footprint of grid G2 with marked locations of 20 NOAA tide gage stations (*numbered labels*); the *red stars* indicate actual tide gages at #1: Sandy Hook and #9 Battery Point, and the *black bullets* mark virtual tide gage locations where corrections are made with respect to the actual gages based on a harmonic analysis (see locations in Table 2). The *red box* marks the footprint of grid G1. Simulated and measured tide time series at the stations are plotted in Fig. 8, and differences between these are quantified in Table 2. Color scale is bathymetry (<0) and topography (>0) in meters referenced to NAVD88 vertical datum

dynamic effects of tides on tsunami inundation and run-up. This is further detailed in Fig. 7b, which shows the envelope of maximum tidal elevations computed in grid G1 during the second tidal cycle (after model ramp-up); there is only a small variation in the maximum tide elevation (less than 0.08 m) from the mouth of the HRE to New York harbor and the East River. As should be expected, maximum elevation gradually decreases in the Hudson River, from Battery Point towards upstream, and maximum elevations are larger in Long Island Sound due to funneling effects. The average maximum elevation computed in grid G1 is +0.72 m NAVD88; looking at Fig. 7b, we see that this level is achieved within ±0.02 m in most of grid G1 (excluding Long Island

Figure 7
Tide simulations in grid G1 (**a**–**c** color scale in meters from NAVD88 datum): **a** bathymetry with marked locations of NOAA tide gage stations (*symbols/numbers*; see Fig. 8 and Table 2 for modeled and reference elevations); **b** envelope of maximum computed tidal elevations; **c** local MHW level calculated with VDatum; **d** friction coefficient C_d; a Manning coefficient $n = 0.025$ was used throughout the domain except in the rivers, where a value $n = 0.015$ was used. The *red line* marked in **a** separates the Hudson River from the Upper New York Bay and is the location of tidal flow rate calculations

Sound, the western part of the Lower Bay, and the upper East River). For comparison, Fig. 7c shows the local MHW level (referenced to NAVD88) computed over grid G1 using NOAA's tool VDatum, which provides an empirical estimate based on values at

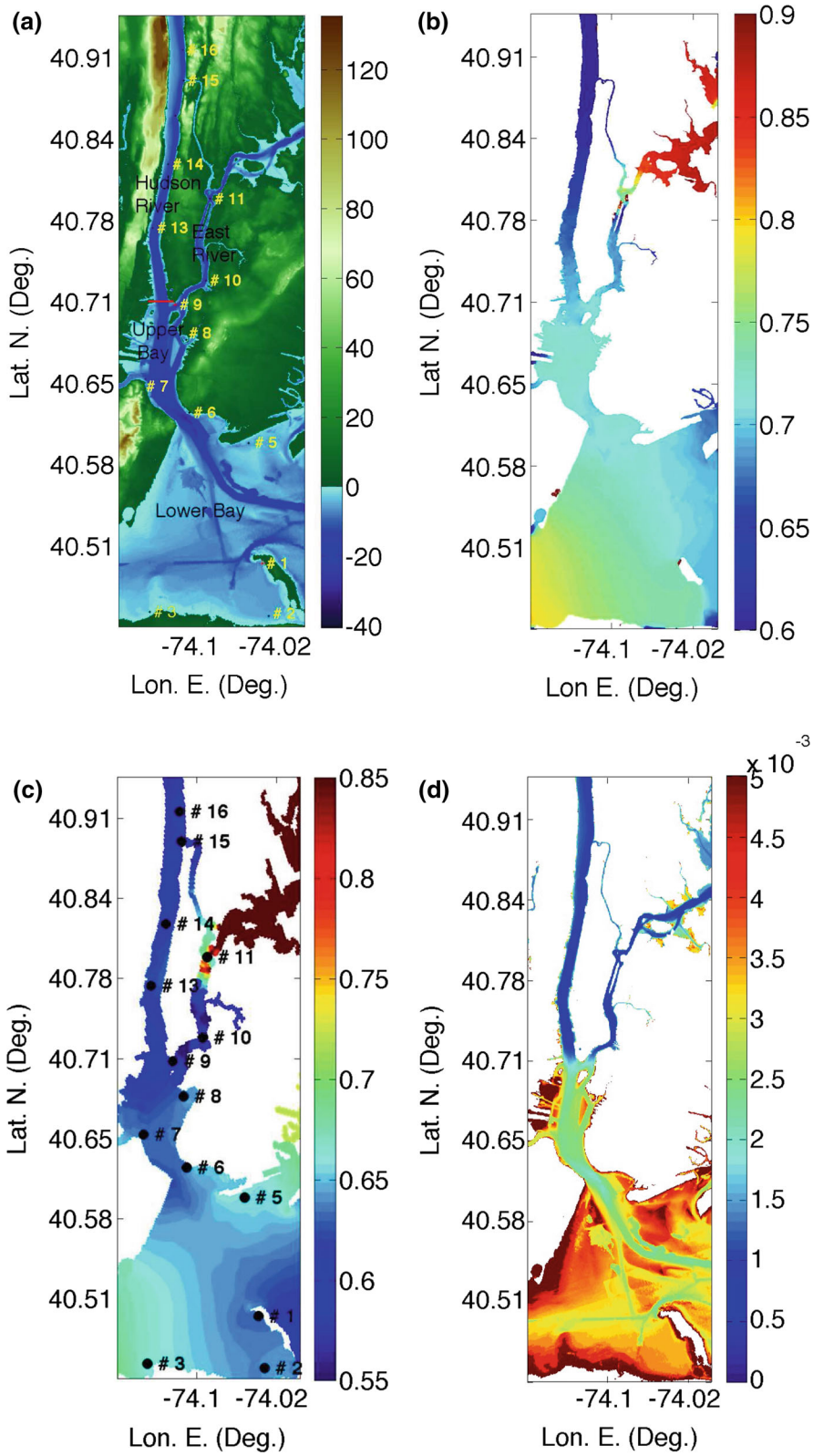
(a)
(b)
(c)
(d)
Lat. N. (Deg.)
Lon. E. (Deg.)
Lon E. (Deg.)
40.91
40.84
40.78
40.71
40.65
40.58
40.51
-74.1
-74.02
Hudson River
East River
Upper Bay
Lower Bay
16
15
14
11
13
10
9
8
7
6
5
1
3
2
120
100
80
60
40
20
0
-20
-40
0.9
0.85
0.8
0.75
0.7
0.65
0.6
0.55
x 10^-3
5
4.5
4
3.5
3
2.5
2
1.5
1
0.5
0

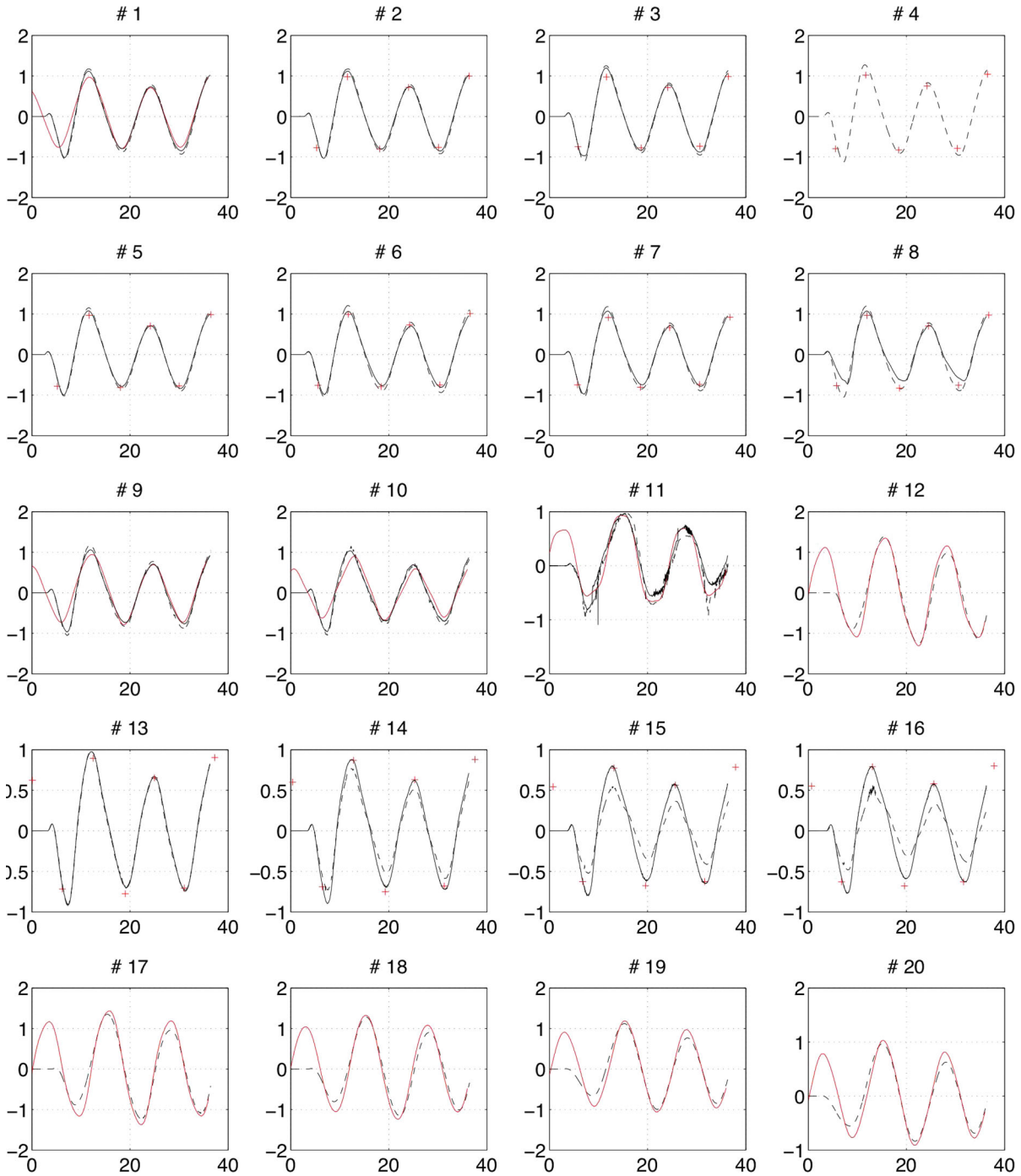

Figure 8
Time series of tidal elevation (with respect to NAVD88) computed with FUNWAVE-TVD in grids G1 (*solid black*) and G2 (*dash black*), at the locations of 20 NOAA tide gage stations (Table 2; Figs. 6 and 7a), compared to NOAA's reference data (*solid red*; either full time series or extrema, whichever is available), for tides from 7:00 am on 13 July 2015 to 7:00 pm on 14 July 2015. The model was initialized in grid G3b with tide results computed with OTPS' model TPXO8. The Manning bottom friction coefficient was calibrated in grids G1 and G2 to achieve a good agreement with the reference data (Fig. 7d; Table 2 compares maximum water levels computed during the second tidal cycle with local MHW levels)

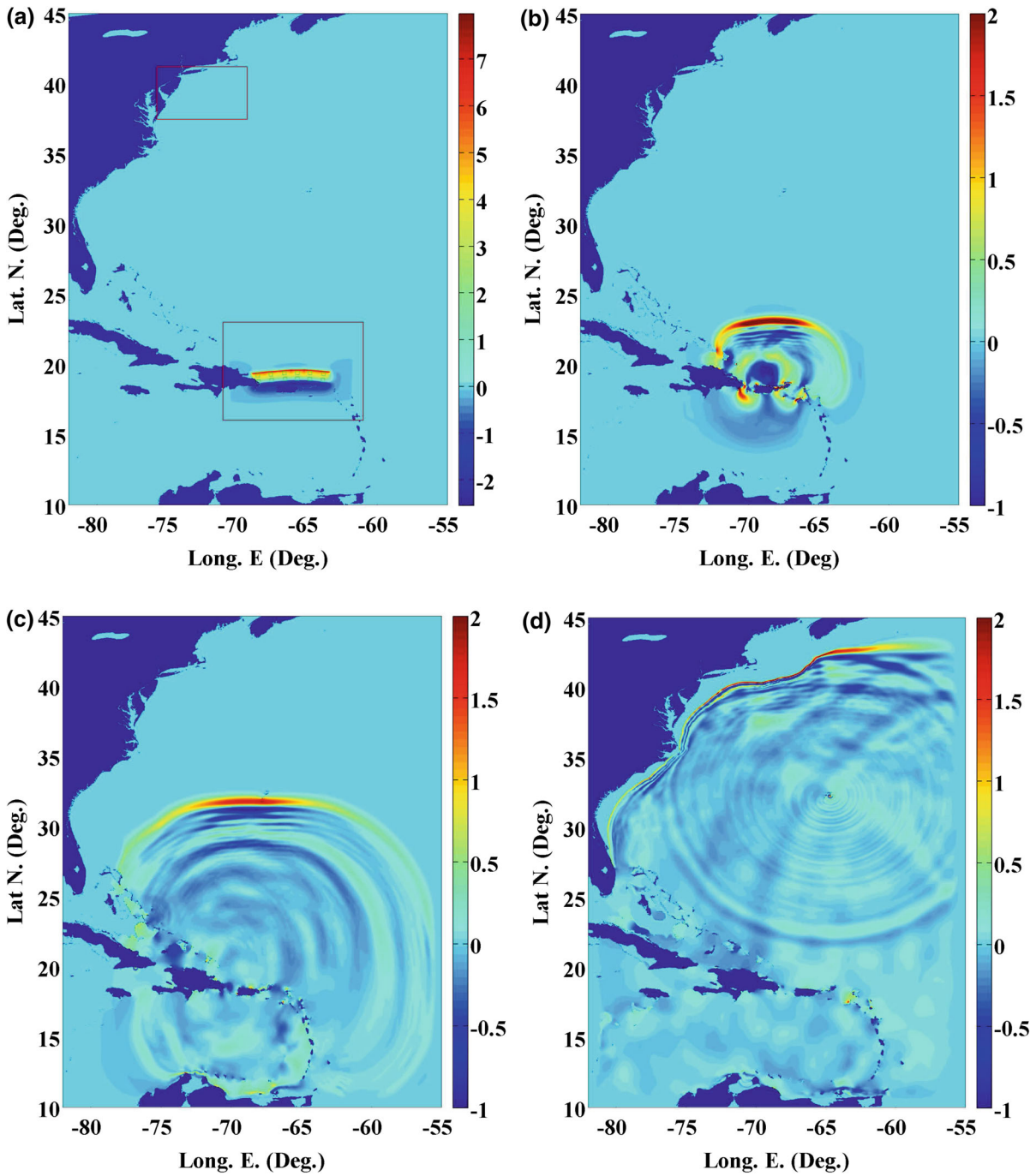

Figure 9
Simulations of the M_w 9 PRT seismic source with FUNWAVE-TVD, in grid G4 (truncated at Lon. E. −55; Fig. 1): **a** Initial surface elevation of tsunami source computed in lower red box with Okada's (1985) method, based on 12 SIFT sub-faults (Gica *et al*. 2008; Grilli and Grilli 2013b); the upper red box approximately represents the area of Fig. 3; **b–d** Instantaneous surface elevations computed after $t = 30$ min, 1 h 42 min and 3 h 20 min of propagation, respectively. All *color scales* are surface elevation in meters

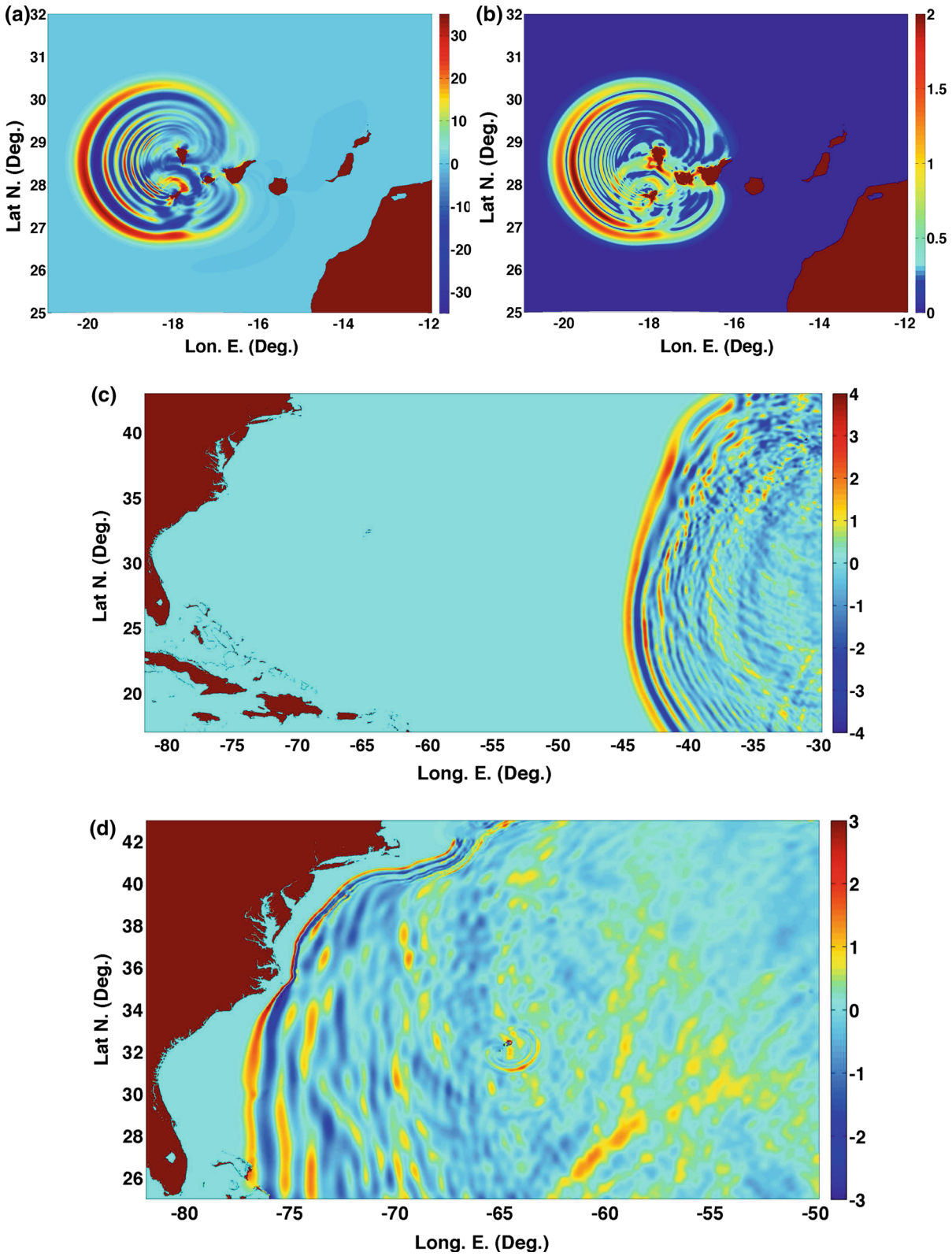
(a)
Lat N. (Deg.)
Lon. E. (Deg.)
(b)
Lat N. (Deg.)
Lon. E. (Deg.)
(c)
Lat N. (Deg.)
Long. E. (Deg.)
(d)
Lat N. (Deg.)
Long. E. (Deg.)

◀Figure 10
Simulations of the 80 km^3 CVV flank collapse source with FUNWAVE-TVD, in grid G4 (Fig. 1): **a**, **b** Surface elevation (m) and horizontal velocity module (m/s), respectively, of tsunami source at $t = 20$ min into the event (Abadie *et al.* 2012) used to initialize FUNWAVE-TVD; **c**, **d** Instantaneous surface elevations after $t = 4$ and 8 h of propagation into the event, respectively, (*color scales* are surface elevation in meters)

reference stations and bathymetry. The pattern of VDatum's MHW values appears to be very similar to that in simulations (Fig. 7b), with values, however, being slightly smaller at most locations; the average of VDatum data is +0.64 NAVD88 (with a standard deviation of 0.02 m), i.e., 0.08 m below that of simulations. This difference, however, is deemed small in view of the uncertainty in VDatum results and other uncertainties, and considering the good agreement of simulations with NOAA's reference data at all the important stations in grid G1.

Results of the tide-only simulations will be used to initialize FUNWAVE-TVD's dynamic tsunami–tide simulations along the boundary of grid G2, in the form of time series of elevations and currents computed in grid G3b. Dynamic tsunami–tide simulations will be compared to tsunami-only simulations performed over a static MHW level. For consistency with NOAA's reference and VDatum data, we will set this level to +0.64 m NAVD88, although the average of maximum tide elevations computed with FUNWAVE-TVD in grid G1 is slightly larger, at +0.72 m; as indicated before, the small difference between these two levels is deemed negligible in view of other uncertainties. Hence, in the tsunami-only simulations, +0.64 m will be added to the bathymetry matrix, creating a geodetic vertical static datum approximately referenced to MHW level. The technique of using a static water level corresponding to MHW in tsunami simulations is consistent with the methodology of Grilli *et al.* (2015b).

4. *Tsunami-only simulations*

Based on earlier work summarized in introduction, three PMTs were selected and propagated into the HRE, as a result of: (1) a far-field M_w 9 seismic source in the Puerto Rico Trench (PRT) (Grilli *et al.* 2010; Grilli and Grilli 2013b; 2) a far-field source from an 80 km^3 partial collapse of the western flank of the Cumbre Vieja Volcano (CVV) in La Palma, Canary Island (Abadie *et al.* 2012; Tehranirad *et al.* 2015) (deemed to be the likeliest extreme collapse scenario; see discussion in introduction); (3) a near-field submarine mass failure (SMF) modeled as a Currituck (CRT) slide proxy on the continental slope, off of the Hudson River canyon (Grilli *et al.* 2015b). The far-field tsunami sources (PRT, CVV) were specified and their propagation was first modeled in grid G4 (Fig. 1), in which time series of boundary conditions were computed to pursue simulations in grid G3b. The near-field tsunami source (CRT SMF proxy) was specified and its propagation first modeled in grid G3a (Fig. 2), in which time series of boundary conditions were computed to pursue simulations in grid G2. In view of the low resolution of bathymetric data used for grids G4 and G3a,b, as recommended by NOAA, no adjustment was made to the reference level in these grids. Simulations in grids G2 and G1 were performed based on a static reference level equal to the local average MHW level in grid G1, +0.64 m NAVD88. In the next section, simulations will be performed in these two grids, dynamically, in combination with the calibrated tide, by superposing tide and tsunami time series as a combined boundary condition along the boundary of grid G2.

Figure 9a shows the initial surface elevation of the M_w 9 PRT tsunami source computed with Okada's 1985 method, based on 12 SIFT subfaults (Grilli and Grilli 2013b; Gica et al. 2008), and Fig. 9b–d shows instantaneous surface elevations computed with FUNWAVE-TVD in the 1 arc-min resolution grid G4 (truncated here at Lon. E. −55 for more efficiency due to the tsunami directionality), after $t = 30$ min, 1h 42 min and 3h 20 min of propagation, respectively. We see that maximum tsunami elevations are quite directional south-to-north and focus on the upper USEC; this was already pointed out by Grilli *et al.* (2010). After 200 min of propagation, the tsunami is entering the SE corner of grid G3b (Fig. 3).

Figure 10a, b shows the surface elevation and horizontal velocity magnitude, respectively, computed by Abadie *et al.* (2012) with the 3D Navier–

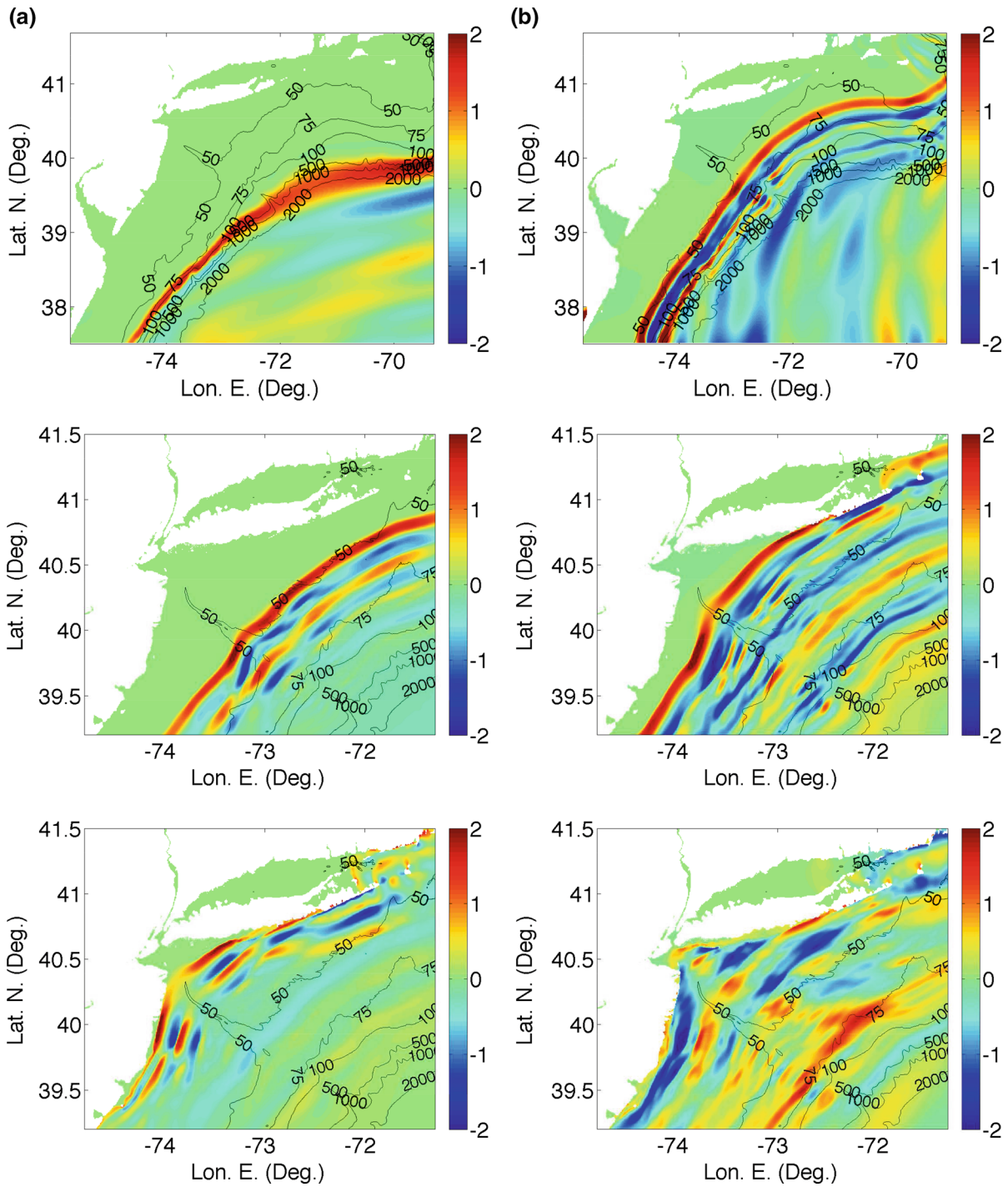

Figure 11
Simulations of far-field tsunami sources with FUNWAVE-TVD. Instantaneous surface elevation in grid G3b (*color scale* is elevation and black contour bathymetry, both in meters), upon reaching the continental shelf, for the: **a** PRT tsunami at $t = 3$, 4 and 5 h and **b** CVV tsunami at $t = 8$, 9 and 10 h since the event, from *top* to *bottom*

Stokes model THETIS for the 80 km^3 CVV flank collapse source, at $t = 20$ min into the event. At this time, surface elevations reach up to 30 m, with the largest values occurring in directions between 15 and 30 deg. south of West, as was already pointed out in other work (Abadie *et al.* 2012; Tehranirad *et al.* 2015). Fig. 10c, d shows instantaneous surface elevations computed with FUNWAVE-TVD in the 1 arc-min resolution grid G4, after $t = 4$ and 8 h of propagation, respectively. These results confirm that maximum tsunami elevations are initially quite directional in a more or less WSW direction towards the Caribbean Islands and South America. Nevertheless, after 8 h of propagation significant tsunami waves of 2–3 m elevation are approaching the upper USEC, entering the SE corner of grid G3b (Fig. 3).

Details of the subsequent propagation of the 2 far-field tsunamis, PRT and CVV, computed in the nested 616-m resolution grid G3b, are shown in Fig. 11a, b, as instantaneous surface elevations at $t = 3$, 4 and 5 h, and 8, 9 and 10 h (since the event), respectively. In each case, the first snapshot is at a time when the tsunami is starting to propagate over the continental shelf; due to refraction, the leading tsunami waves have gradually become more or less parallel to the

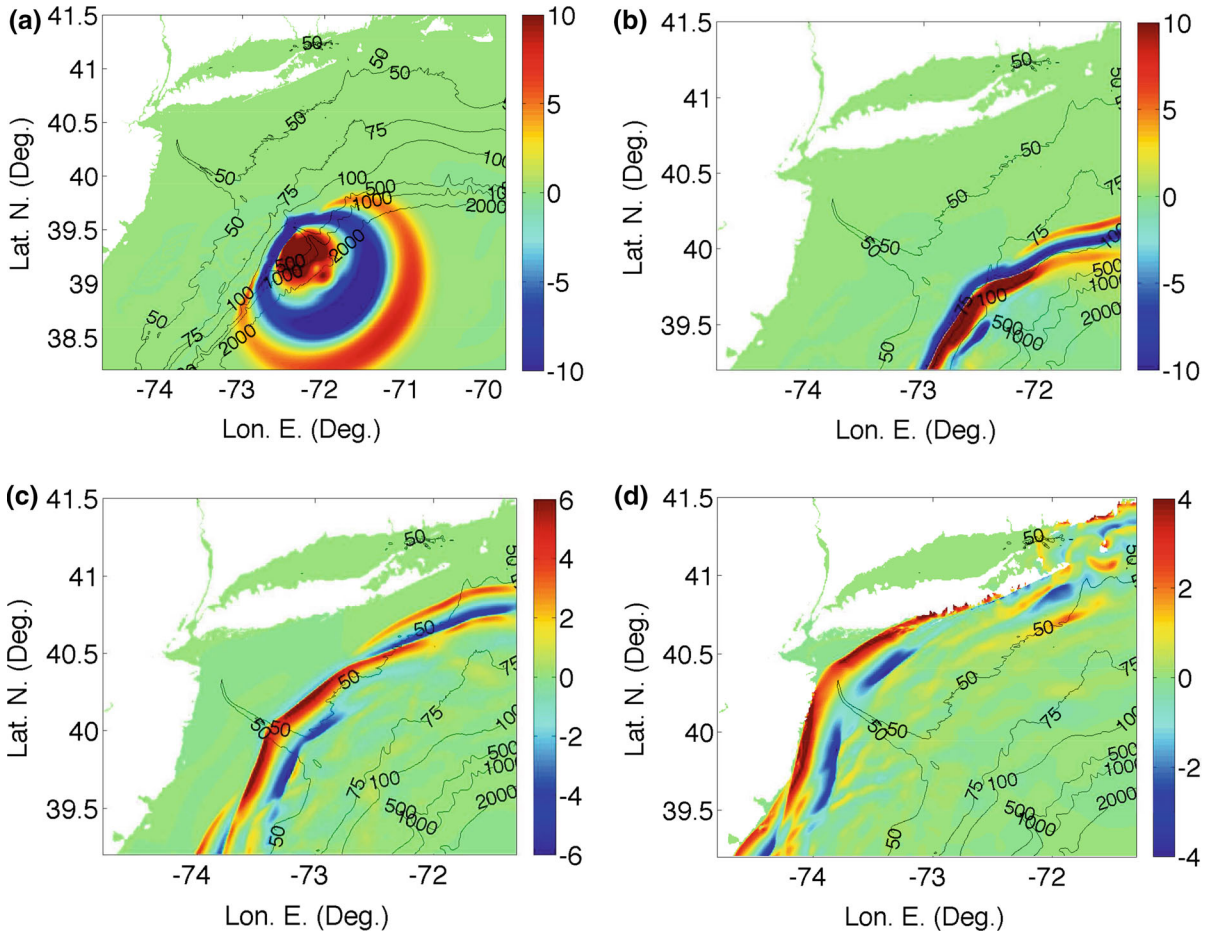

Figure 12
Simulation with FUNWAVE-TVD of near-field Currituck (CRT) SMF proxy tsunami source located in Study Area 1 (Fig. 2), off of the Hudson River canyon. **a** SMF tsunami elevation generated with NHWAVE (Ma *et al.* 2012; Grilli *et al.* 2015b) at $t = 13$ min, used to initialize FUNWAVE-TVD. Surface elevations simulated in grid G3a (*color scale* is elevation and black contour bathymetry, both in meter) at $t =$ **b** 30 min, **c** 1 h 18 min and **d** 2 h 8 min into the event

local isobaths. Hence, the very different initial directionality of the propagation of these tsunamis (i.e., approximately from south to north for PRT and east to west for CVV) has been lost during refraction over the shelf slope. This property of long wave refraction was analyzed in more details for the CVV tsunami by Tehranirad *et al.* (2015), who performed simple ray tracing analyses and showed the strong bathymetric control on near-shore tsunami propagation, causing waves to focus on or defocus away from specific areas of the coastline. In particular, here we see that in both cases incident waves refract away from the Hudson River canyon and focus on the shores of eastern New Jersey and western Long Island (NY). Partial reflection occurs along these shores and reflected waves interact later in time with other waves in the incident wave trains, creating more complex patterns offshore (see, e.g., Fig. 11b bottom panel).

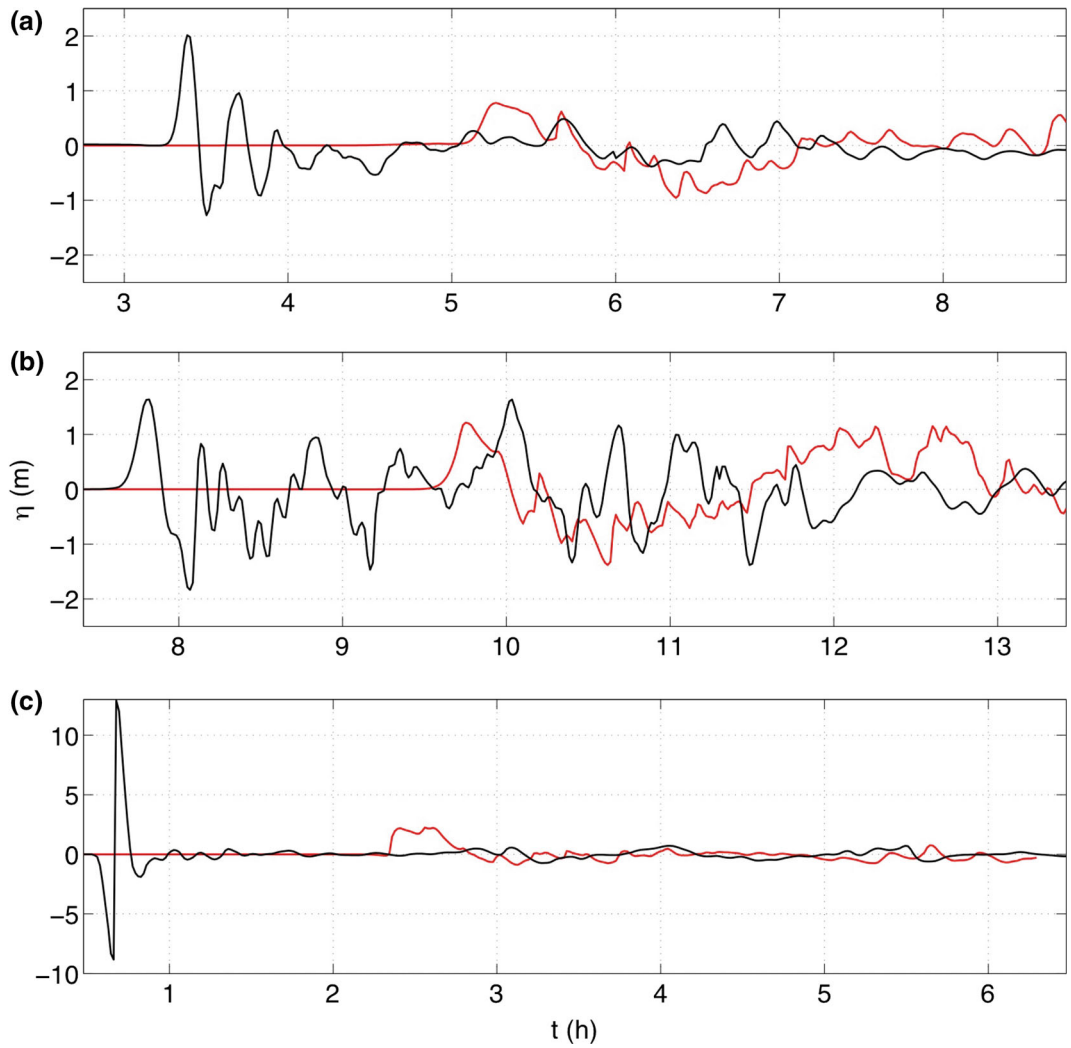

Figure 13
Time series of surface elevations computed with FUNWAVE-TVD in grid G2 (time in hour is from the start of each respective event): (*red solid lines*) at the entrance of Lower Bay along the eastern boundary of grid G1 (−73.944 Lon. E., 40.501 Lat. N.; see location in Fig. 5), and (*black solid lines*) at the SE corner of grid G2 (Table 1), for the propagation of each incident PMT, over a +0.64 m (NAVD88) static level (approximating the local MHW level): **a** PRT ; **b** CVV; and **c** CRT SMF proxy

Figure 12a shows the surface elevation for the near-field Currituck (CRT) SMF proxy source sited in Study Area 1 (Fig. 2) off of the Hudson River canyon, interpolated in the 616-m resolution grid G3a, at $t = 13$ min into the event. This source was computed using the 3D non-hydrostatic model NHWAVE (Ma *et al.* 2012; Grilli *et al.* 2015b) and its elevation and corresponding horizontal velocity (not shown here) were used to initialize FUNWAVE-TVD's simulations in grid G3a. At the time of Fig. 12a, the tsunami caused by the SMF features a large leading depression wave (about -10 m) moving into the Hudson River Canyon, followed by a larger (15 m) elevation wave. Other waves in the wave train are propagating offshore (to the SE). Upon propagation (not shown here), these shorter dispersive waves develop an oscillatory tail of higher frequency waves. The onshore propagation of the CRT tsunami is detailed in Fig. 12b–d, which shows instantaneous surface elevations computed at $t = 30$ min, 1 h 18 min and 2 h 8 min into the event, respectively. Similar to the PRT and CVV cases, the shelf bathymetry induces a strong refraction of incoming tsunami waves, which gradually become parallel to local isobaths as they approach shore, as for the other two cases, waves are refracted away from the Hudson River Canyon and

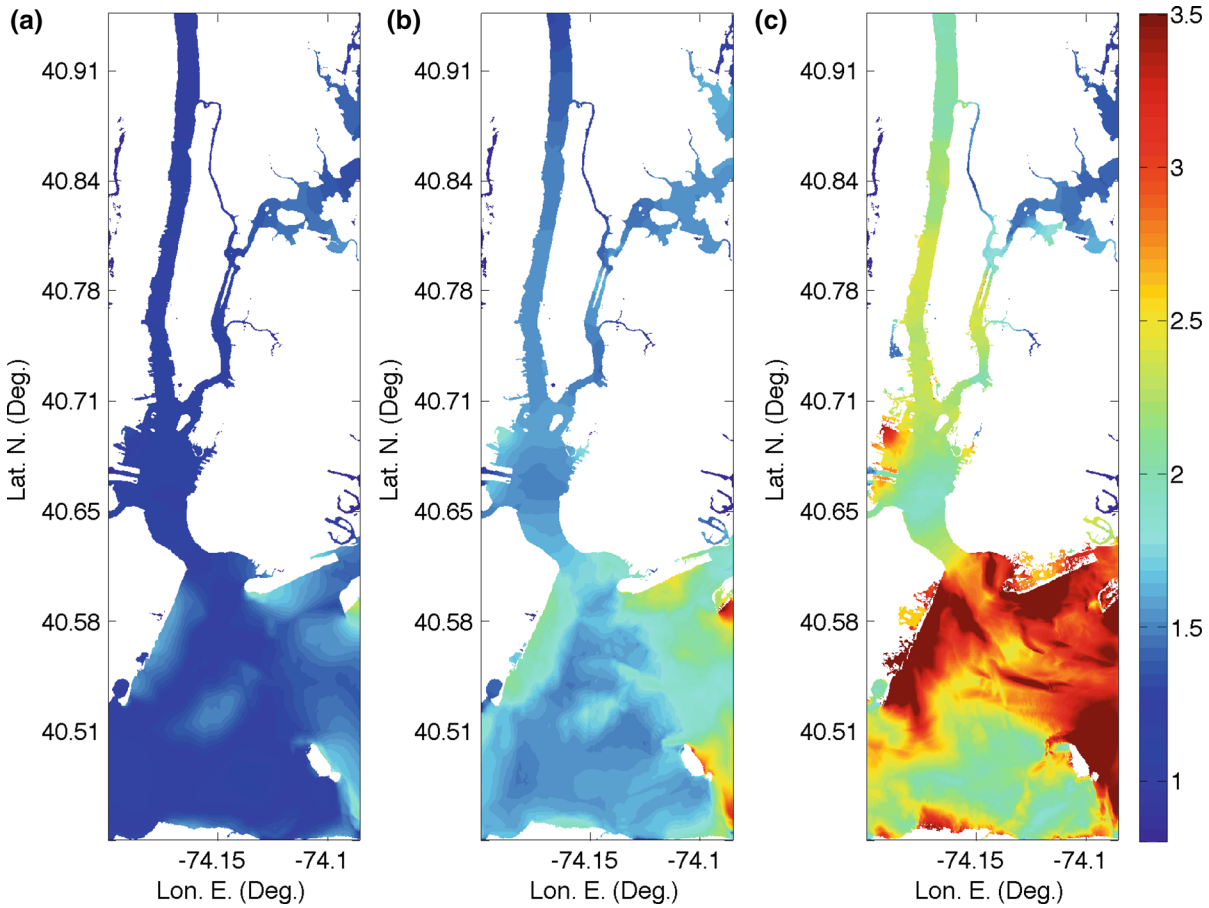

Figure 14

Envelope of maximum surface elevations (*color scale* in meters) computed with FUNWAVE-TVD in grid G1, for the propagation of each incident PMT over a +0.64 m NAVD88 static level (approximating the local MHW level). To more accurately plot tsunami elevations over the local MHW level, results were corrected by the local difference between the static level and that obtained with VDatum (shown in Fig. 7c): **a** PRT (up to $t = 9$ h); **b** CVV (up to $t = 13.5$ h); and **c** CRT SMF proxy (up to $t = 6.5$ h). *Times in parenthesis* indicate the total duration of tsunami simulations from the start of each respective event

focused on shores located on either sides of it, where partial reflection occurs.

Simulations of the propagation of the three incident tsunamis (PRT, CVV, CRT) are pursued into the HRE with FUNWAVE-TVD, by one-way coupling, first in the 154-m resolution nested grid G2, using results of grids G3a,b as boundary conditions, and then similarly in the 39-m resolution nested grid G1 (Figs. 3, 6, 7a). Figure 13 shows time series of surface elevations computed in grid G2 relative to the static water level for the three incident tsunamis, at a numerical gage located at the entrance of Lower Bay along the eastern boundary of grid G1 (-73.944 Lon. E., 40.501 Lat. N, local depth 16.9 m; see location in Fig. 5). For comparison, similar time series are plotted at a gage located on the SE corner of grid G2, in deeper water (78 m depth; Table 1). At grid G2's SE corner: (1) the PRT tsunami has a leading 2-m elevation crest followed by 2 large waves (with height of about 2.3 and 1.3 m, respectively, and an 18-min period) and a tail of smaller oscillations; (2) by contrast, the CVV tsunami, which also has a leading crest with 1.6 m elevation, has a tail of more than 6 large long waves (of height 1.2–2.9 m and period 21–42 min), over which many shorter wavelength (higher frequency) waves are superimposed (with period 4–6 min), as a result of dispersion (Tehranirad *et al.* 2015); finally (iii) due to the proximity to its source (Fig. 12a), the CRT SMF proxy tsunami is a large dipole wave of 6.5-min period with a leading depression of −9 m followed by a 12-m crest. After propagating over the shallow shelf from grid G2's SE corner to Lower Bay's entrance, for about 1h 45 min, Fig. 13 shows that each tsunami wave train has significantly transformed, with wave elevations decreasing and some waves being damped out; maximum surface elevation for the PRT, CVV and CRT tsunamis have reduced to 0.8, 1.2 and 2 m, respectively. This results from the combination of energy spread out, due to wave refraction over the Hudson River Canyon bathymetry (see Figs. 11, 12), and energy dissipation due to bottom friction. Tehranirad *et al.* (2015) confirmed the significant effect of bottom friction on long wave propagation over a wide shallow shelf by comparing model results with an analytical solution.

Surface elevations for the entire propagation of the 3 tsunamis (in grids G3a,b, G2 and G1) are

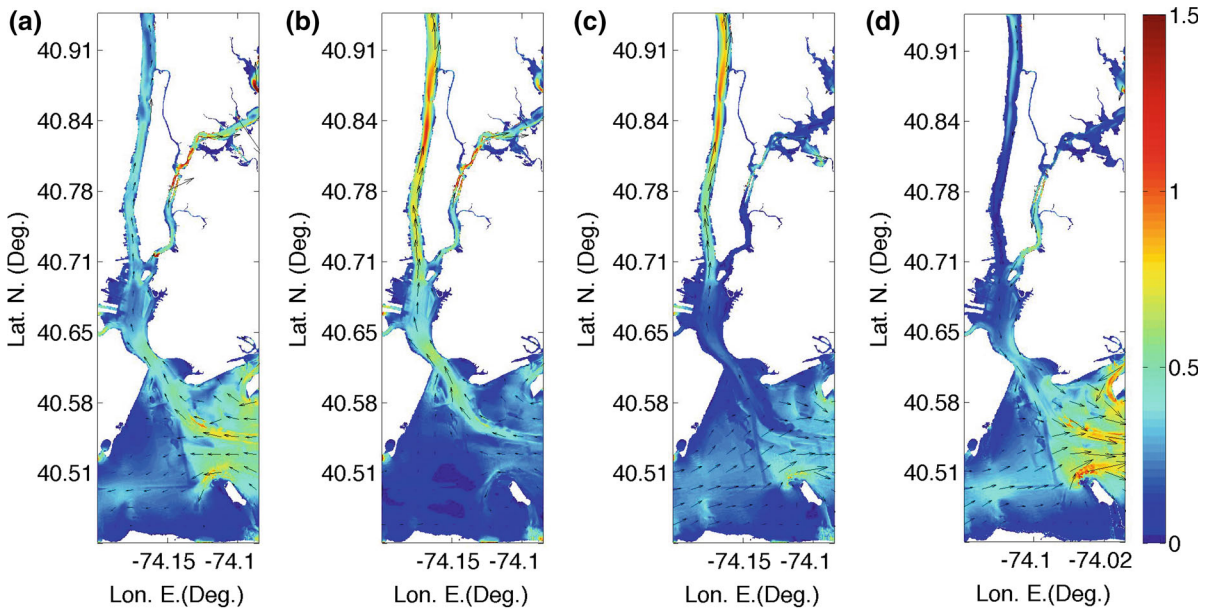

Figure 15
Magnitude (*color scale* in m/s) and direction (vectors) of tidal currents computed with FUNWAVE-TVD in grid G1, for four phases of the calibrated tide reaching MHW level at its highest elevation. Tide phases correspond to the tide arriving at Sandy Hook station #1 (Table 2; Fig. 6): **a** 1.5 h before; **b** concurrent with; **c** 1.5 h after; and **d** 3 h after high tide

provided as supplementary online material, in the form of animations of model results: PRT.mp4, CVV.mp4, CRT.mp4. These show details of wave refraction, dissipation, and reflection off the coast during tsunami propagation over the shelf bathymetry (grids G3a,b), as well as tsunami propagation into the HRE and resulting flooding. [Note, for the CRT case, as can be seen in the animation between $t = 31'19''$ and $36'20''$, to avoid using unnecessary wide sponge layers in grid G3a, the offshore moving part of the tsunami was truncated; this, however, does not affect the tsunami wave train propagating onshore towards the mouth of the HRE.] Animations in grid G1 are provided as side-by-side panels for both a static reference level, as discussed here, and dynamic tsunami–tide simulations, which are detailed in the next section. Besides color-coded elevations, these animations also show the instantaneous total current (i.e., tsunami plus tide if simulated dynamically) in the form of velocity vectors.

Envelopes of maximum surface elevation and inundation caused by each PMT in the HRE are plotted in Fig. 14, based on results in grid G1. It should be noted that, to allow for a better comparison

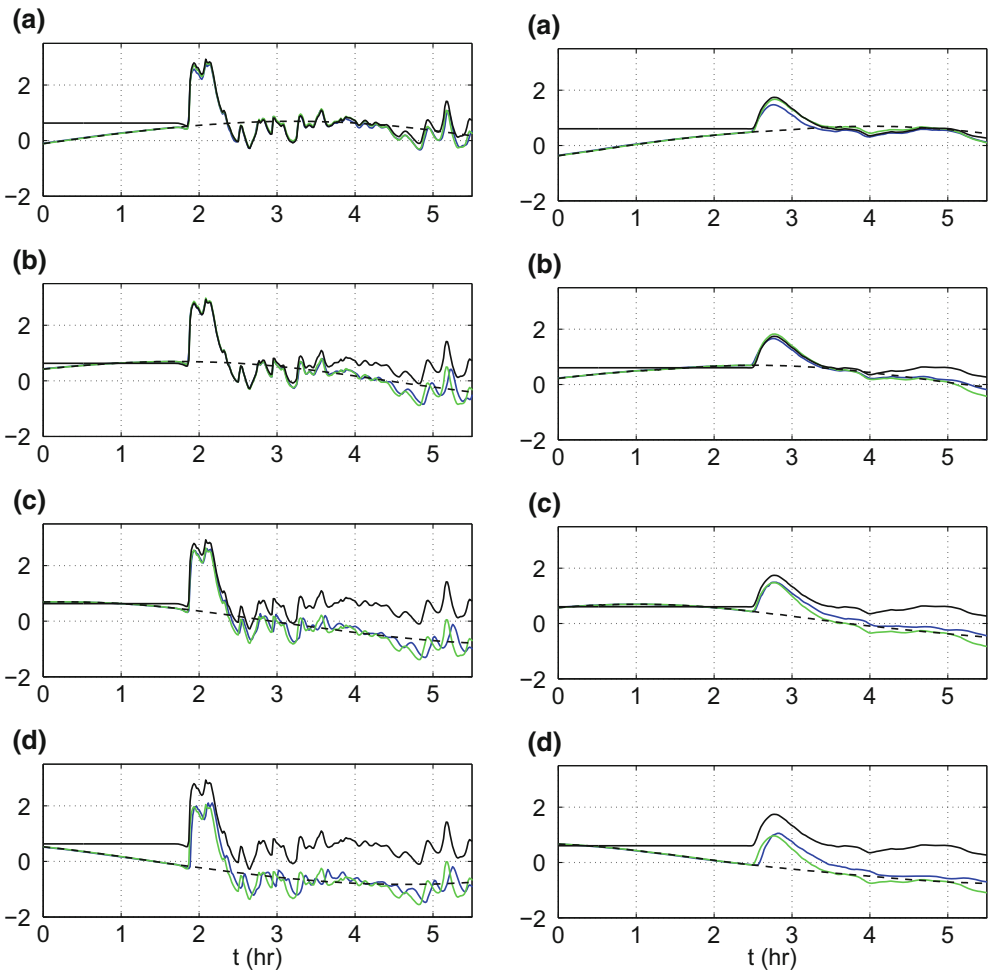

Figure 16
Time series of surface elevations (in meter referenced to NAVD88) computed for the CRT SMF proxy tsunami at the entrance to Lower Bay (*left*) and Battery Point (*right*) (stations #1 and #3 in Fig. 17): (*blue lines*) dynamic tsunami–tide simulations; (*black lines*) tsunami simulations over a +0.64 m static MHW level; (*green lines*) linear superposition of tide and static tsunami simulations (tide elevations are shown as dashed lines for reference). Dynamic simulations were performed for the leading tsunami crest arriving at Sandy Hook station at four phases of the tide (see Fig. 15): **a** 1.5 h before, **b** concurrent with, **c** 1.5 h after, and **d** 3 h after high tide

with the dynamic results, plots in the figure were computed from the results of tsunami propagation over the static MHW level (+0.64 m NAVD88; equal to the domain-averaged MHW), slightly corrected by the local difference between this averaged level and the actual space-varying MHW obtained with VDatum (shown in Fig. 7c), which at most locations is within a few centimeters of the maximum elevation of the calibrated tide (shown in Fig. 7b). In each case, maximum surface elevations in the HRE are found to be consistent with surface elevations computed at the entrance of Lower Bay (Fig. 13). For PRT, maximum coastal inundation/runup are 1 to 2 m, and for CVV these are 1.3–2.5 m; for CRT, surface elevations are divided into two regions: (1) outside of New York Harbor, coastal inundation/runup are 2–3.5 m in most areas; (2) inside the harbor (including along the coast) maximum elevations are 1.5–2 m.

5. *Dynamic tsunami–tide simulations*

Simulations are repeated for the three incident PMTs in combination with the time-varying calibrated tide, which both modulates the reference water level and causes a significant pre-existing as well as time-varying current. This tide was calibrated for its maximum elevation to closely match the local MHW level in the area of grid G1. To identify conditions leading to maximum inundation, we consider various phases of the tide at the time of tsunami arrival in Lower Bay.

In deeper water, offshore of the HRE, both tide and tsunamis are long waves of fairly small amplitude, as compared to depth and wavelength, which can thus be linearly combined (i.e., both elevation and current are additive) (Dean and Dalrymple 1991). For such a superposition to be accurate closer to shore, water depth must be large enough compared to tsunami and tide elevation; here, considering that incident tsunami amplitudes are in the order of 2 m or less (Fig. 13) and tide amplitudes are up to 1 m (Fig. 8), water depth should be on the order of at least 20 m. As indicated before, incident tides computed in grid G3a and tsunamis computed in grid G3b are linearly combined at numerical gages (stations) located along the offshore boundary of grid G2. Figure 5 shows that water depth is greater than 30 m at these gages, except for a few located on the northernmost part of the grid eastern boundary in Long Island, and the westernmost part of the grid southern boundary in New Jersey. Since these shallower areas are fairly small parts of the grid boundary, located far away from the entrance to the HRE (Fig. 5), potential nonlinear effects caused by a

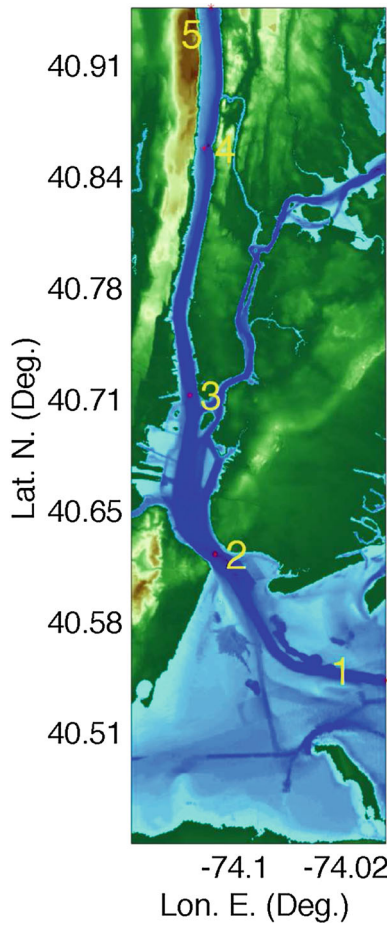

Figure 17
Locations in the HRE of numerical gages/stations #1 to 5 (*red stars*) where time series of surface elevations and currents are computed in grid G1, to perform the more detailed analysis of tsunami–tide interactions. See Figs. 16, 24, 25, 26, 27, 28 and 29 for results

linear superposition of tide and tsunami signals are deemed negligible for simulations in the HRE. Along the offshore boundary of grid G2, tsunami-induced currents for the 3 PMTs are found to be 3–20 times larger than the maximum tidal currents, which supports their linear superposition. For each considered tsunami–tide combination, once computations are completed in grid G2, these are pursued in grid G1 by one-way coupling, as was done for the tsunami simulations over a static water level. All simulations were performed using the same Manning friction coefficients as in the tide- and tsunami-only simulations.

Linear tsunami–tide combinations are specified along the boundary of grid G2 for four phases of the tidal signal, i.e., a minimum of four simulations are performed for each incident tsunami to identify the combination of tidal elevations and currents that best enhances the incident tsunamis and causes the maximum combined tsunami–tide elevations and coastal inundation in grid G1. These phases were selected such that the leading and/or maximum crest of each tsunami arrived at Sandy Hook, NJ (station #1 in Fig. 7): (1) 1.5 h before, (2) concurrent with, (3) 1.5 h after, and (4) 3 h after high tide. The 1.5-h time interval between each combination roughly represents one-eighth of the dominant tidal period. For the PRT and CRT tsunamis, tsunami–tide synchronization was done for the leading crest (Fig. 13). For the CVV tsunami, a second taller crest arrived just over two hours after the initial crest (Fig. 13); accordingly, besides four simulations for the leading crest, four additional dynamic simulations were performed for CVV, corresponding to the arrival of this second crest at the four phases of the tide.

Figure 15 shows the magnitude and direction of tidal currents computed in the HRE for the four selected phases of the calibrated tide. Panel a, 1.5 h

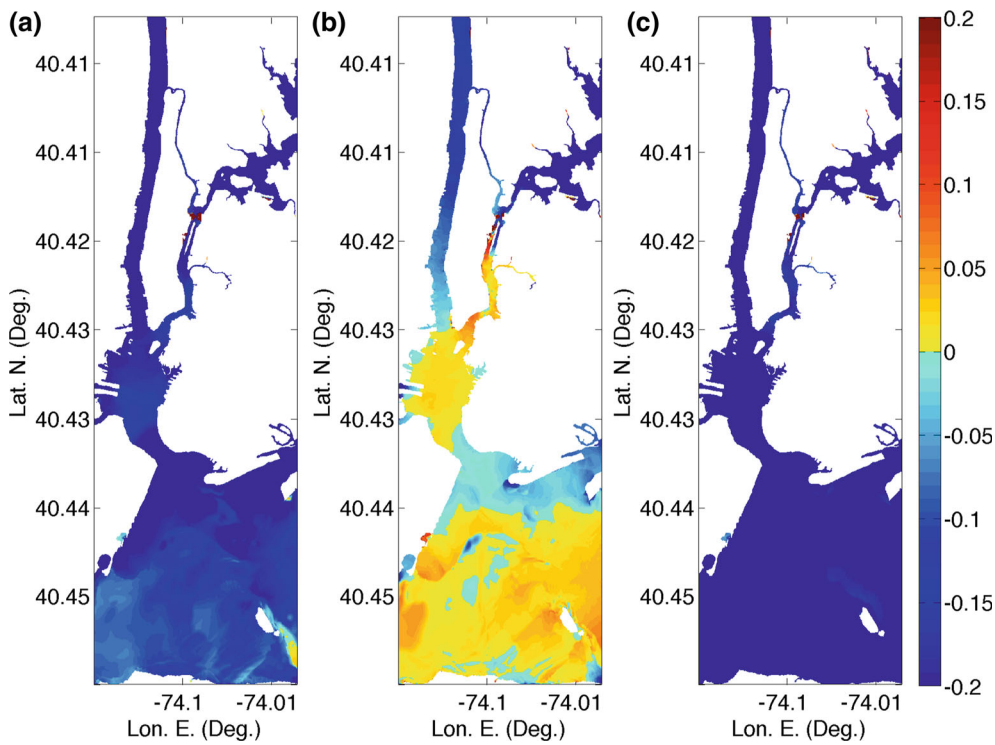

Figure 18

Differences (*color scale* in meters) between envelopes of maximum surface elevation computed in grid G1, for the PRT tsunami over dynamic and static (Fig. 14) tide levels (the latter are corrected to match the local MHW computed with Datum). The initial tsunami crest arrives at the Sandy Hook station #1 (Table 2; Fig. 6): **a** 1.5 h before; **b** concurrent with; and **c** 1.5 h after high tide

before high tide, corresponds to the strongest flood currents. At high tide, in panel b, weaker currents are still flowing into the Lower Bay, the Hudson and East Rivers, with currents being larger in the central channel. In panel c, 1.5 h after high tide, while strong currents are still flowing into the Hudson River, the East River is at slack, and strong currents are ebbing out of Lower Bay. Finally, in panel d, 3 h after high tide, ebbing currents are flowing out of Lower Bay and the rivers, and are strongest near the mouth of the Bay. In this simulation, the strongest currents nearly reach 1.5 m/s (3 knots), which is notably larger (more than twice) than the currents simulated by TAJALLI-BAKHSH *et al.* (2014) (and observed) in the wider Chesapeake Bay and even in the James River.

In view of these current patterns, one might anticipate that the second and third phases of dynamic tsunami–tide simulations, in which the largest wave in each incident tsunami reaches the Sandy Hook gage, near the mouth of the HRE, concurrently or 1.5 h after high tide, should lead to the maximum amplification of the incident tsunamis, at least, near the mouth of the Bay. Indeed, while for these phases tidal elevations are either maximum or have not yet decreased too much from their highest level, the tsunamis propagating into the Lower Bay will be facing opposite (ebbing) currents that will be increasing or be already quite strong (0.5– 0.75 m/s in Fig. 15c); these opposite currents will continue to strengthen as the tsunamis propagate into New York Harbor and the Hudson and East Rivers (as seen in Fig. 15c, d) and should cause the tsunami surface elevation to rise, at least initially. In Fig. 15d, while currents are even stronger 3 h after high tide, tide surface elevations are starting to become negative and hence it will be harder to achieve higher elevations in the combined results. Although we will keep computing this fourth phase of the tide to establish envelopes, its results will not be further detailed.

Being both long waves, without nonlinear interactions, tide and tsunami should be propagating into the HRE at the same phase speed and their combined level should evolve in a way similar to the individual levels. Nonlinearity, however, will affect these features, first by causing amplitude dispersion effects that will move the maximum of the combined

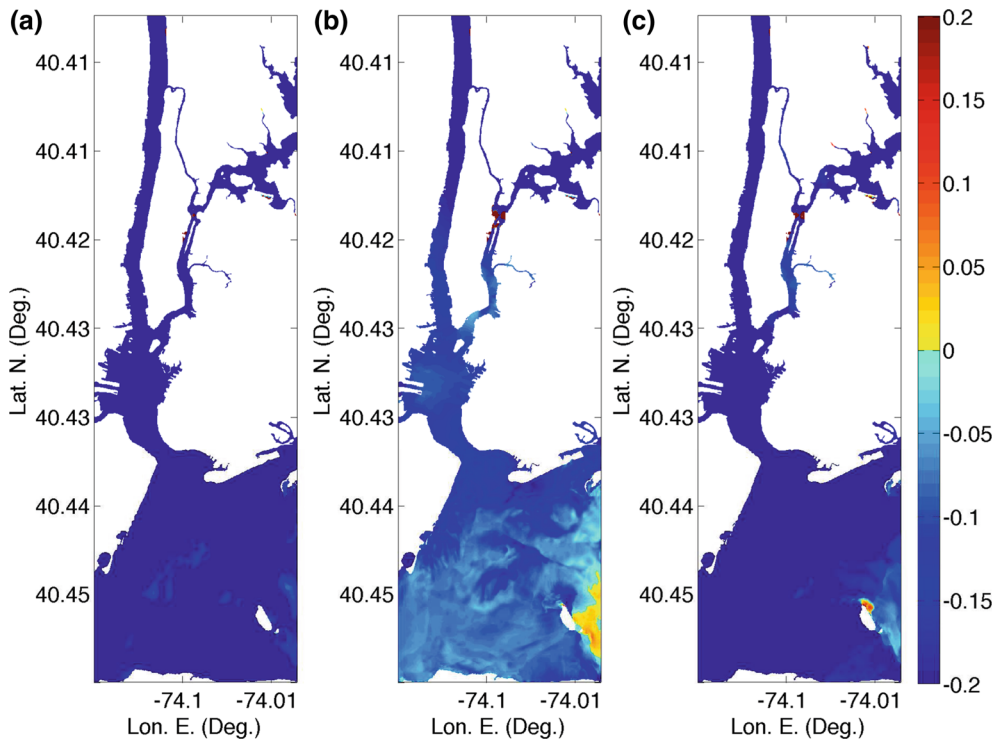

Figure 19
Same as Fig. 18 for the maximum crest of the CVV tsunami

elevations ahead or behind the initially combined values, as well as amplification of the tsunami elevation by opposing (ebbing) currents and vice versa. Additionally, the larger/lower currents occurring near the seafloor in the dynamic tsunami–tide simulations will cause more/less dissipation of the tsunami by bottom friction. To identify and quantify nonlinear effects, results of each dynamic tsunami–tide simulation will be compared to those of the corresponding simulation done over a static water level equivalent to the space-averaged MHW level in grid G1 (+0.64 m NAVD88). Specifically, maximum and instantaneous computed surface elevations, and time series of those and of corresponding currents at selected reference gages, will be compared across grid G1.

Figure 16 compares surface elevations computed in the dynamic and static simulations for the CRT SMF proxy tsunami, which causes the largest incident tsunami in the HRE, at the entrance of Lower Bay and at Battery Point (stations #1 and #3 in Fig. 17), for the four selected phases of the tide. Additionally, the linear superposition of the calibrated tide with the tsunami elevations is also plotted, which allows quantifying the importance of nonlinear interactions. [As before, static simulation results were slightly adjusted to the local MHW based on VDatum data, to illustrate the competing effects of a fluctuating mean water level (MWL) and opposing tidal currents.] At the entrance to Lower Bay (station #1), the surface elevation of the leading tsunami crest in the linear combination exceeds that of the dynamic simulation while the tide current is co-flowing [(i.e., when the tsunami arrives 1.5h or less before high tide: cases (a) and (b)]. When the current starts ebbing [cases (c) and (d)], the elevation of the dynamic tsunami–tide simulation gradually exceeds that of the linear combination. This pattern is also observed at Battery Point (station #3). Hence, the expected effect of an opposing current to enhance the leading tsunami crest is indeed predicted in the dynamic simulations. Figure 16 also shows that, at both stations, the simulation over a static MHW level yields a larger absolute surface elevation of the leading tsunami crest than the dynamic simulations,

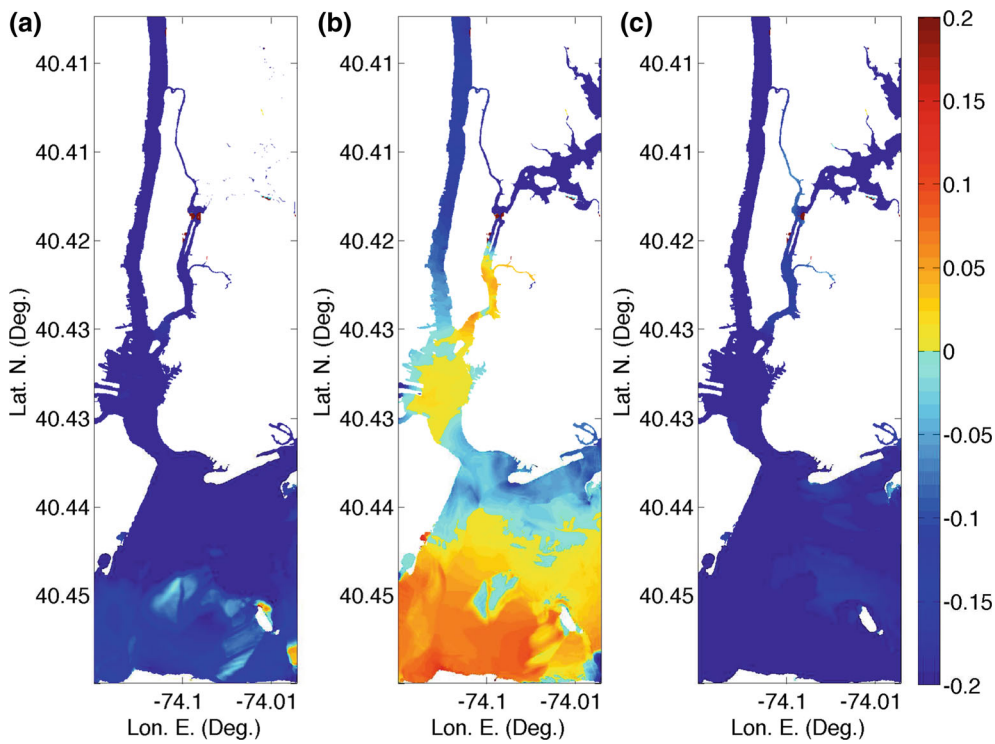

Figure 20
Same as Fig. 18 for the leading crest of the CVV tsunami

for all tide phases except case (b), when the tsunami arrives at high tide. Here, the elevation of the dynamic simulation slightly exceeds that of the static simulation for part of the time series. Results and differences between static and dynamic simulations are further detailed below.

Thus, Figs. 18, 19, 20 and 21 show differences of maximum envelopes of surface elevations computed for the dynamic tsunami–tide and the static MHW level simulations, for the PRT, CVV (both leading and maximum crest cases), and CRT tsunamis, respectively. Results are shown for the dynamic combinations corresponding to the selected tsunami crest arriving at three tidal phases: (1) 1.5 h before; (2) concurrent with; and (3) 1.5 h, after high tide. For PRT, Fig. 18 shows that the worst dynamic case scenario as far as coastal flooding is when the leading tsunami crest arrives at high tide at the Sandy Hook station, causing an increase in inundation in the HRE by 0.03–0.07 m, up to Battery point. For CVV, when synchronizing the largest crest in the tsunami wave train with the tide, Fig. 19 shows that the worst dynamic case scenario is also for high tide, leading to a slightly increased flooding, by up to 0.05 m at the entrance to Lower Bay. Upon entering Lower Bay, this crest interacts with tidal currents that have already been disturbed by more than 2 h of tsunami propagation into the bay and reflection coming back from the upper part of the HRE. The confused currents within the Bay are likely responsible for the mild decrease (by up to −0.05 m) in surface elevation seen across the remainder of grid G1. This is confirmed in Fig. 20, where instead the slightly smaller leading crest of the CVV tsunami was synchronized with the same 4 tide phases. Despite the lower crest, the dynamic simulation at high tide predicts inundations that exceed the static case by 0.05–0.1 m, up to the East River. Finally, Fig. 21 shows that the dynamic simulations of the CRT SMF proxy tsunami cause the largest increases in coastal flooding, by up to 0.15 m, again for the same high-tide phase. Unlike the other two PMTs, however, the largest increases in

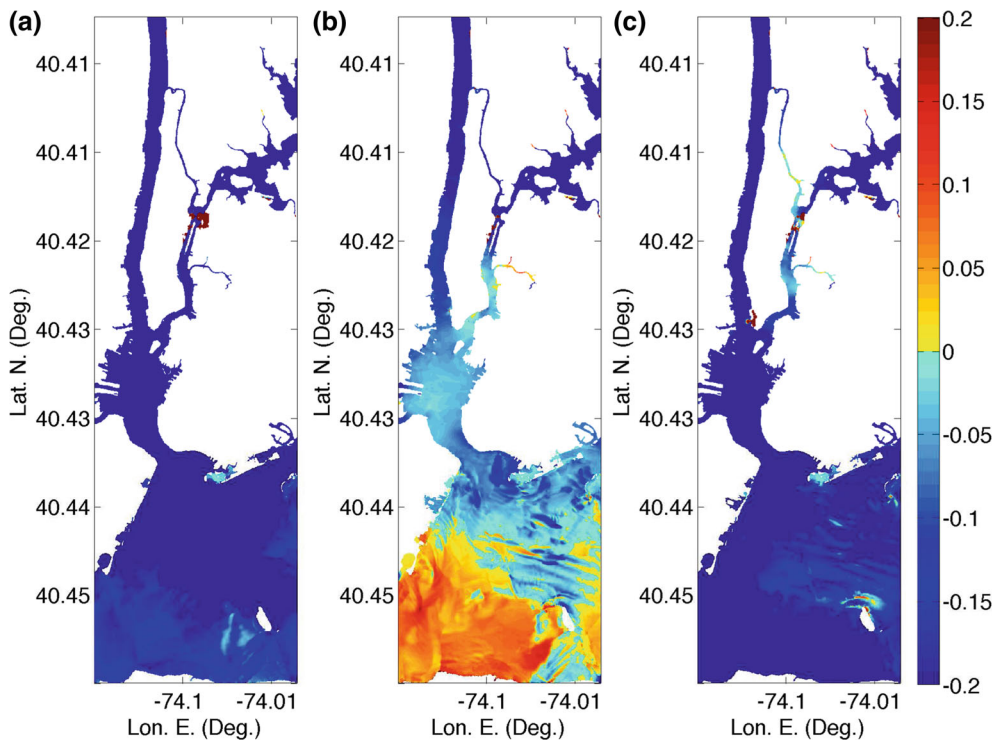

Figure 21
Same as Fig. 18 for the CRT SMF proxy tsunami

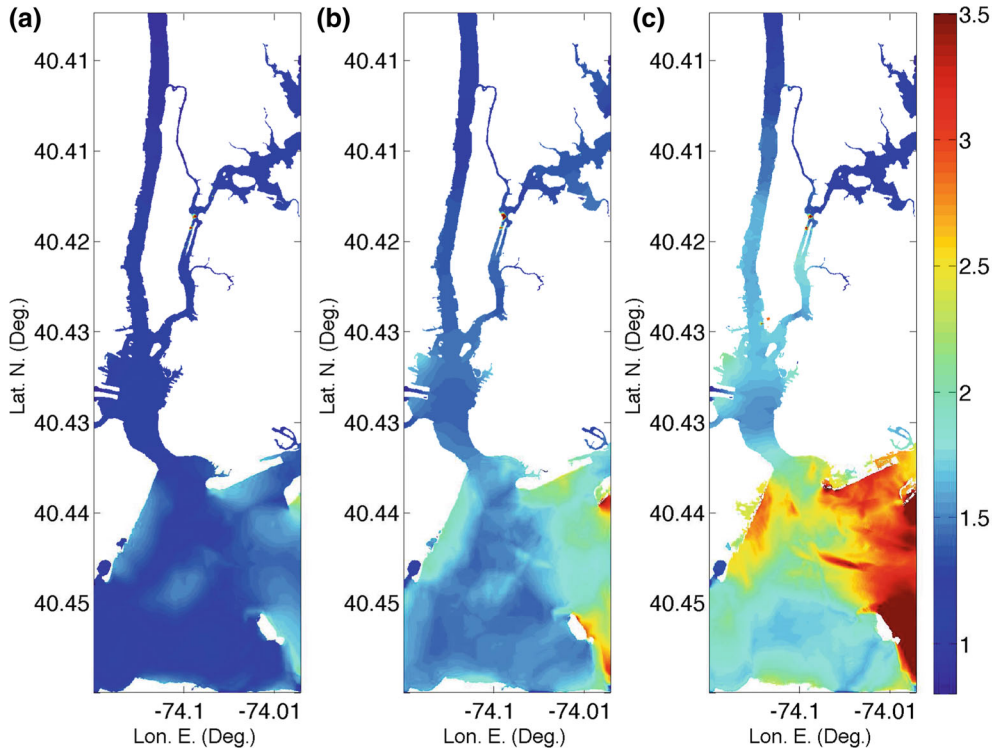

Figure 22

Envelope of maximum surface elevations (*color scale* in meter) computed for the propagation of each incident PMT into grid G1, over a dynamic tide (approximating the local MHW level at its highest elevation), over the four tested tide phases (arriving at Sandy Hook station #1 (Table 2; Fig. 6) 1.5 h before, concurrent with; 1.5 h after, and 3 h after high tide): **a** PRT (up to $t = 9$ h); **b** CVV (up to $t = 13.5$ h); and **c** CRT SMF proxy (up to $t = 6.5$ h). *Times in parenthesis* indicate the total time of tsunami simulations since the start of each respective event

surface elevation are observed in the southern portion of Lower Bay and no or a negligible increase is observed in the Upper Bay.

As an overall summary of tsunami flooding hazard in the HRE, Figure 22 shows the maximum envelopes of surface elevations computed for each PMT over the four tested tide phases (i.e., the dynamic simulations on which the difference plots of Figs. 18, 19, 20 and 21 are based, plus the 3 h delay case), and their difference with the envelope of the same results over a static MHW level (Fig. 14) is plotted in Fig. 23. [Note, as before, eight tide cases (four for each of the two large crests) are included in the CVV dynamic envelope in Fig. 22.] These results confirm that dynamic tsunami–tide interactions can cause a slightly increased flooding in the HRE (by up to 0.15 m), especially in the southern and southwest regions of Lower Bay, and in Battery Point and the East River around Manhattan. It also appears that the increase in flooding associated with the leading crest of the longer period far-field tsunamis (PRT and CVV) occurs relatively farther inland than that of the shorter period near-field tsunami (CRT). While Fig. 16 shows that much of the higher frequency content of the CRT tsunami signal is filtered out by the time waves reach Battery Point, the lower frequencies of the PRT and CVV tsunamis are able to penetrate deeper.

As mentioned before, animations of model results for the three PMTs propagating into grids G3a,b, G2

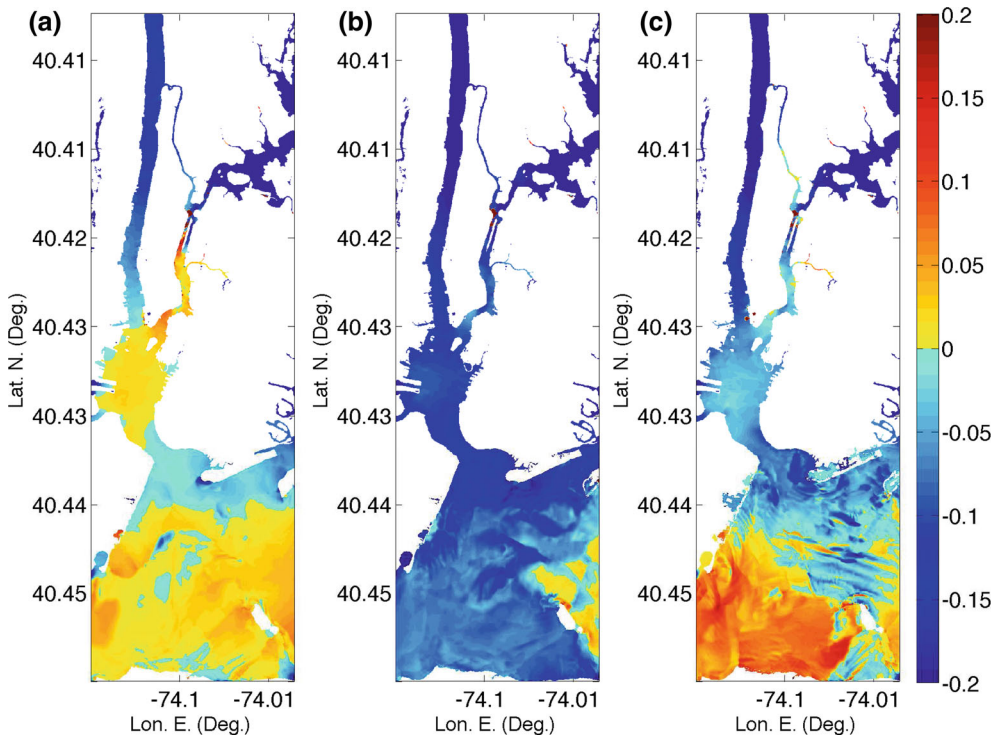

Figure 23
Difference of maximum surface elevation (*color scale* in meter) computed over grid G1 for the: **a** PRT; **b** CVV; and **c** CRT tsunamis, between the envelope of dynamic tide (envelope of envelopes for the four tested tide phases; Fig. 22) and static tide computations (Fig. 14; the latter are corrected to match the local MHW computed with Datum)

and G1 are provided as supplementary online material: PRT.mp4, CVV.mp4, CRT.mp4. These more clearly show where the largest surface elevations occur in the HRE and their magnitude and phase. In grids G2 and G1, animations are based on results of dynamic tsunami–tide simulations for the case of each tsunami arriving at the Sandy Hook gage (station #1) concurrently with high tide. Results discussed above indicate that this represents the worst case (flooding) scenario at most locations. In grid G1, the animations show two side-by-side panels, one for the dynamic simulations and the second one, for comparison, for tsunami propagation over the static MHW level. Results in grid G1 also show instantaneous currents as velocity vectors (i.e., side-by-side for tsunami alone or combined tsunami–tide currents), which allows more easy understanding of how the tsunami velocity field is spatially modified. Currents are further detailed and analyzed in the next section.

6. Detailed analysis of results and discussion

Results presented above indicate that tsunami–tide interactions may lead to increased flooding and stronger currents in some areas of the HRE, depending on tide phase, although this effect appears to be small on maximum flooding. Here, we further analyze the physical mechanisms governing these interactions on the basis of time series of currents (Figs. 24, 25, 26) and surface elevations (Figs. 27, 28, 29) computed at 5 numerical gages (marked in Fig. 17), from the entrance of Lower Bay to the upper part of the Hudson River. Results are from simulations in the finer resolution grid G1, for the 3 PMTs combined with the three main phases of the tide considered so far, i.e., 1.5 h before, concurrent with, and 1.5 h after high tide, plus the 3h after high tide phase, to have a case with stronger ebbing currents. Note that here currents have been projected in the local main

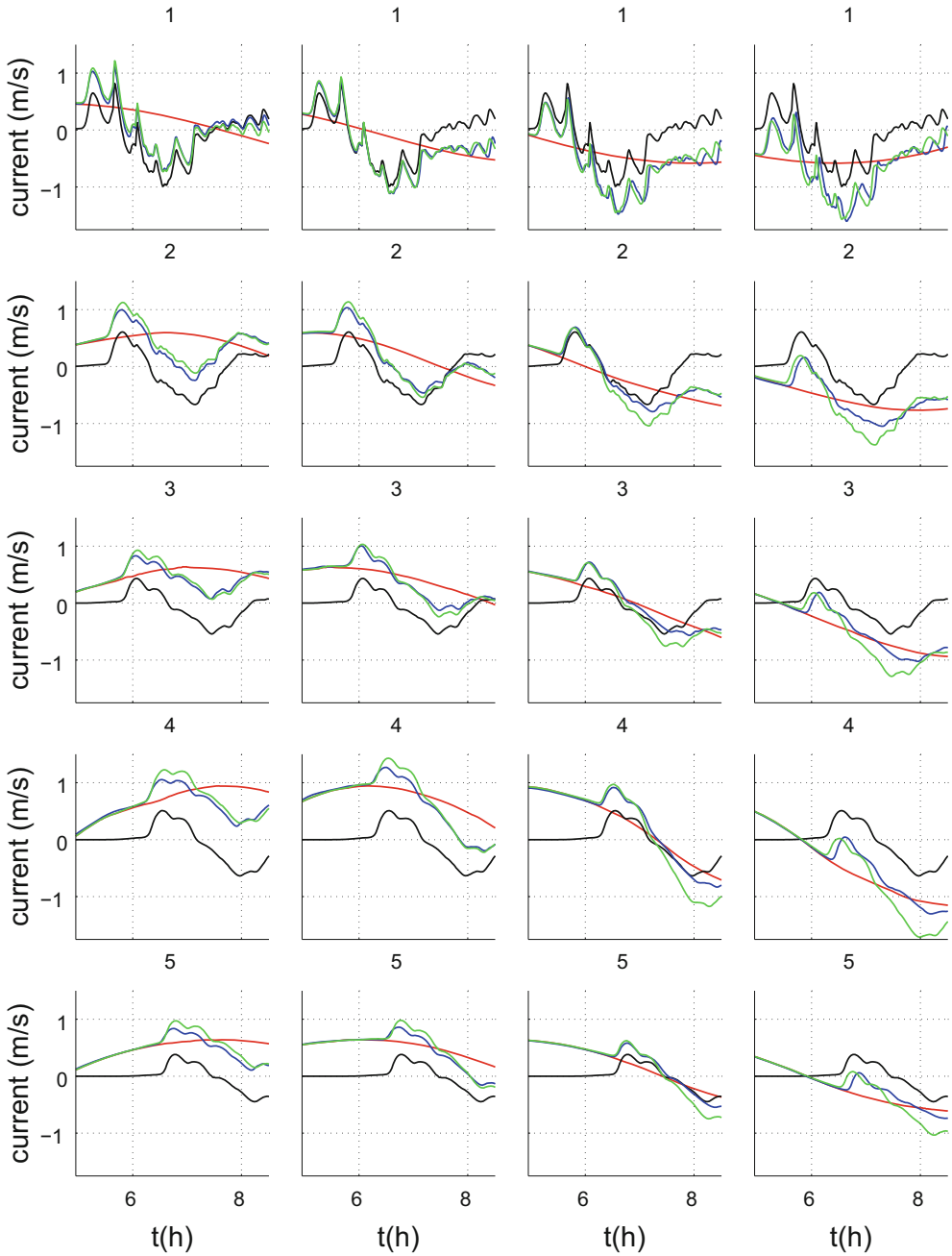

Figure 24
Time series of currents computed in grid G1, at stations #1–5 (labels; Fig. 17) (projected in the tsunami direction of propagation), for the PRT tsunami (*black*), tide (*red*), and their linear (*green*) and nonlinear (*blue*) combinations: 1.5 h before, concurrent with, 1.5 h after and 3 h after high tide, from leftward to rightward columns. Time is measured from the beginning of the event

direction of tsunami propagation at each station. In Figs. 24, 25 and 26, we compare currents computed in the dynamic (nonlinear) tsunami–tide simulations, the static tsunami simulations over an MHW level, and the linear superposition of the corresponding tide and tsunami currents. For surface

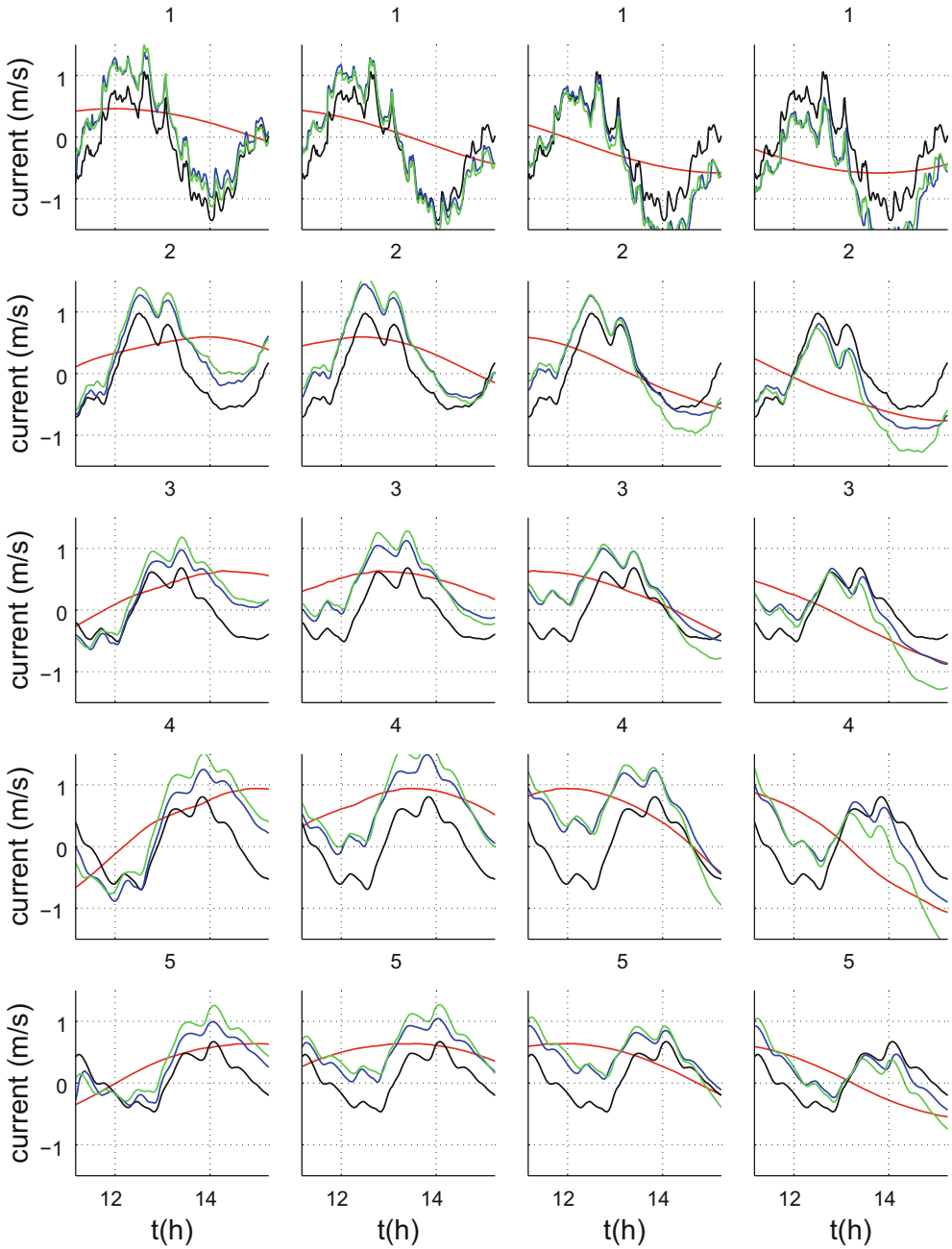

Figure 25
Same results as in Fig. 24 for the CVV tsunami

elevations in Figs. 27, 28 and 29, we compare the detided dynamic and static results; detiding is done by subtracting the corresponding tide surface elevations (MHW or dynamic level, depending on the considered case).

Figures 24, 25 and 26 show similar current patterns for the three tsunami cases, which have the expected behavior. At all stations, when the tide is co-flowing (flooding current), the nonlinearly combined tide and tsunami currents are either equal to or

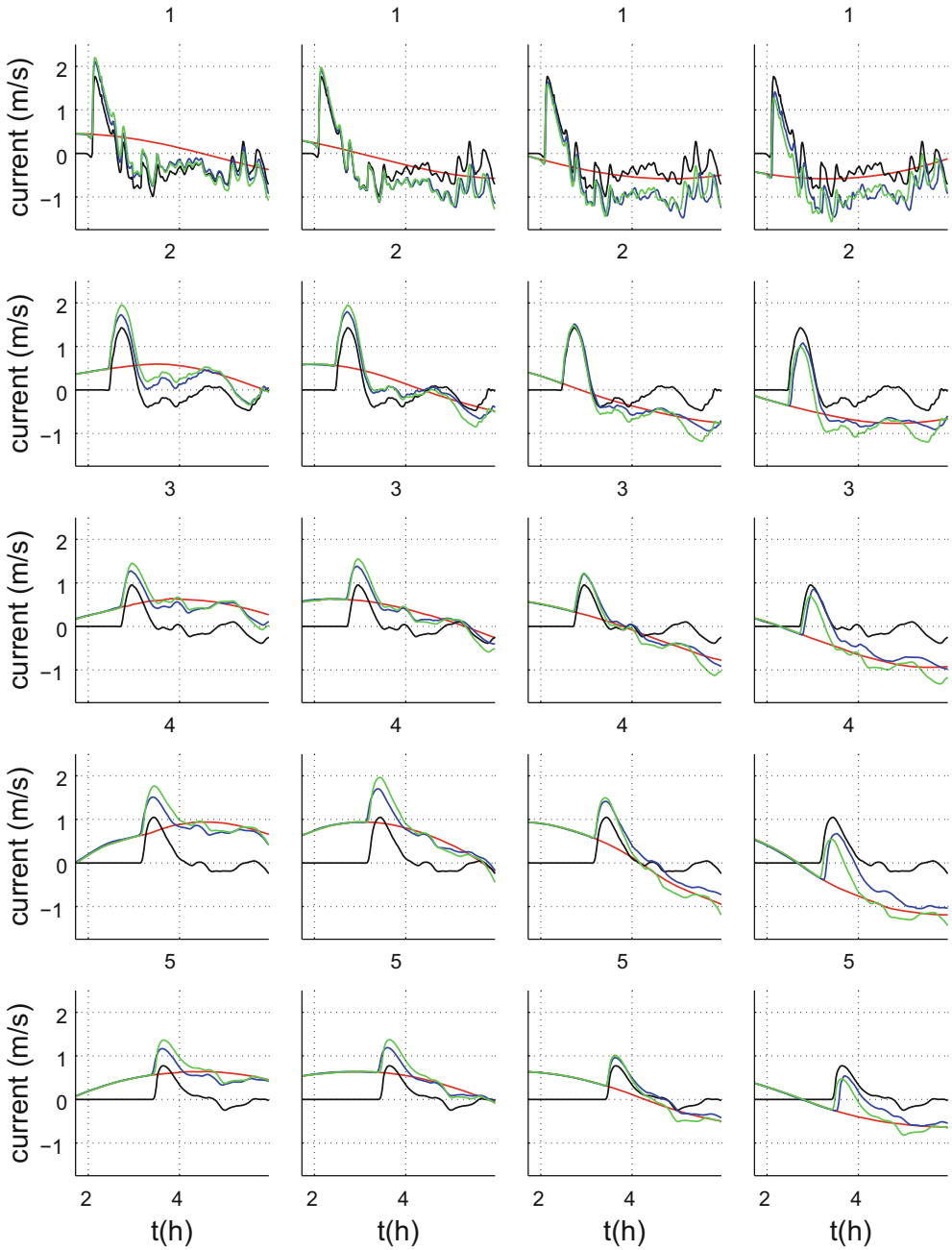

Figure 26
Same results as in Fig. 24 for the CRT SMF proxy tsunami

have a slightly smaller magnitude than the linearly combined currents, likely as a result of the increased bottom friction dissipation. When the tide is opposite (ebbing current), this trend reverses itself and the nonlinearly combined currents become larger than the linearly combined currents. For the selected tide phases, however, which are aimed at maximizing the combined tsunami–tide elevations, the latter mostly occurs in the tail of the tsunami wave trains and, as we shall see, when surface elevations are lower; hence, the impact on maximum flooding is minimal. In all cases, higher frequency oscillations seen in the

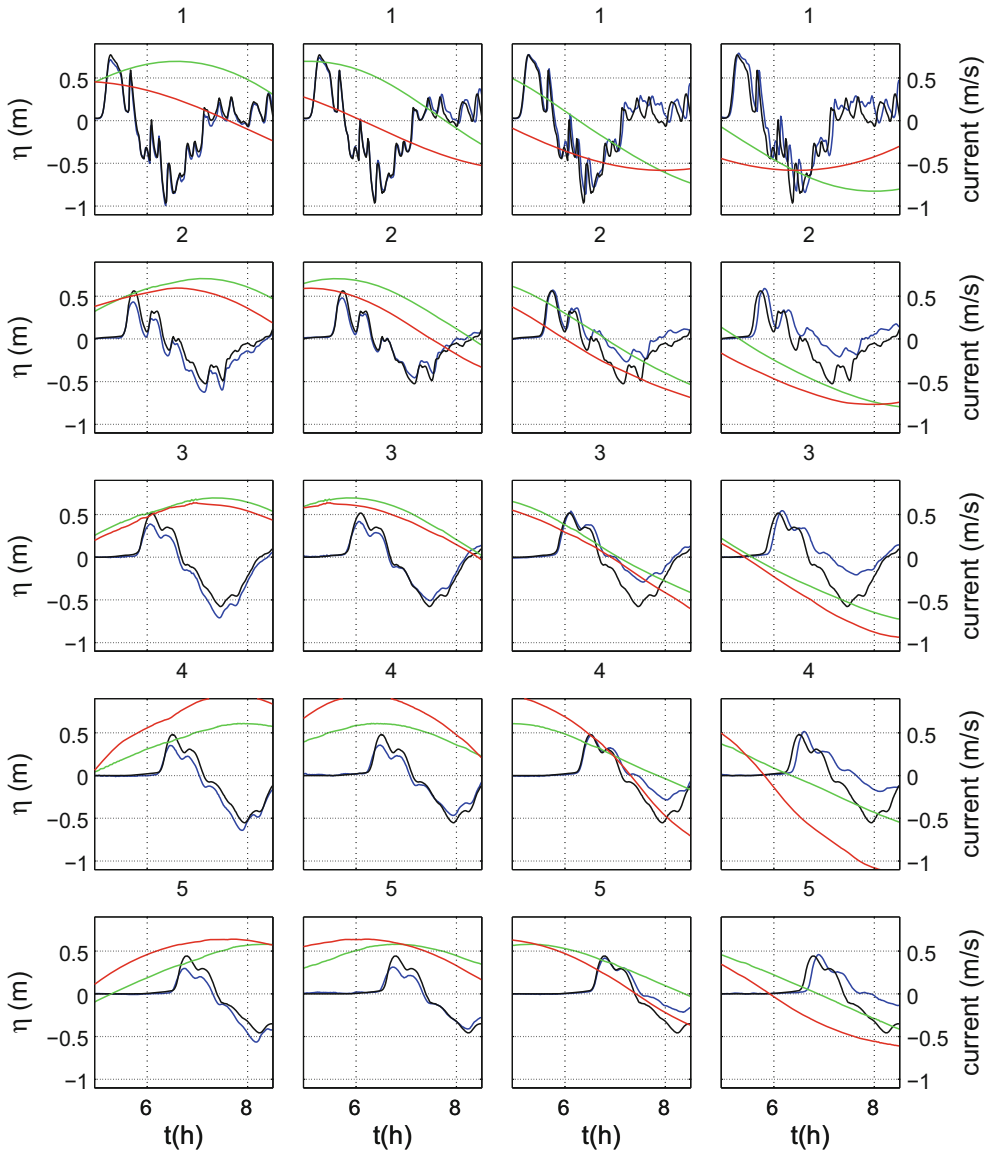

Figure 27
Time series at stations #1–5 (labels) in grid G1 (Fig. 17) of tidal currents projected in the tsunami direction of propagation (*red*), and surface elevations for the tide (*green*), and PRT tsunami: over the static MHW level (*black*), and in dynamic combination with the tide (*blue*): 1.5 h before, concurrent with, 1.5 h after and 3 h after high tide, from leftward to rightward columns. Tsunami surface elevations (static and dynamic) have been detided by subtracting the corresponding tide surface elevations (i.e., static MHW level or dynamic level). Time is measured from the beginning of the event

incident tsunami currents are gradually damped as the tsunamis propagate up the estuary, also likely as a result of dissipation by increased bottom friction. Most of this damping happens by the time the tsunamis reach station #2. A slightly early arrival of tsunami currents is observed in the dynamic case when there is a favorable (co-flowing) tidal current, which indicates an increase in wave phase velocity; consistent with this, a later arrival is observed for ebbing currents and this difference in arrival time

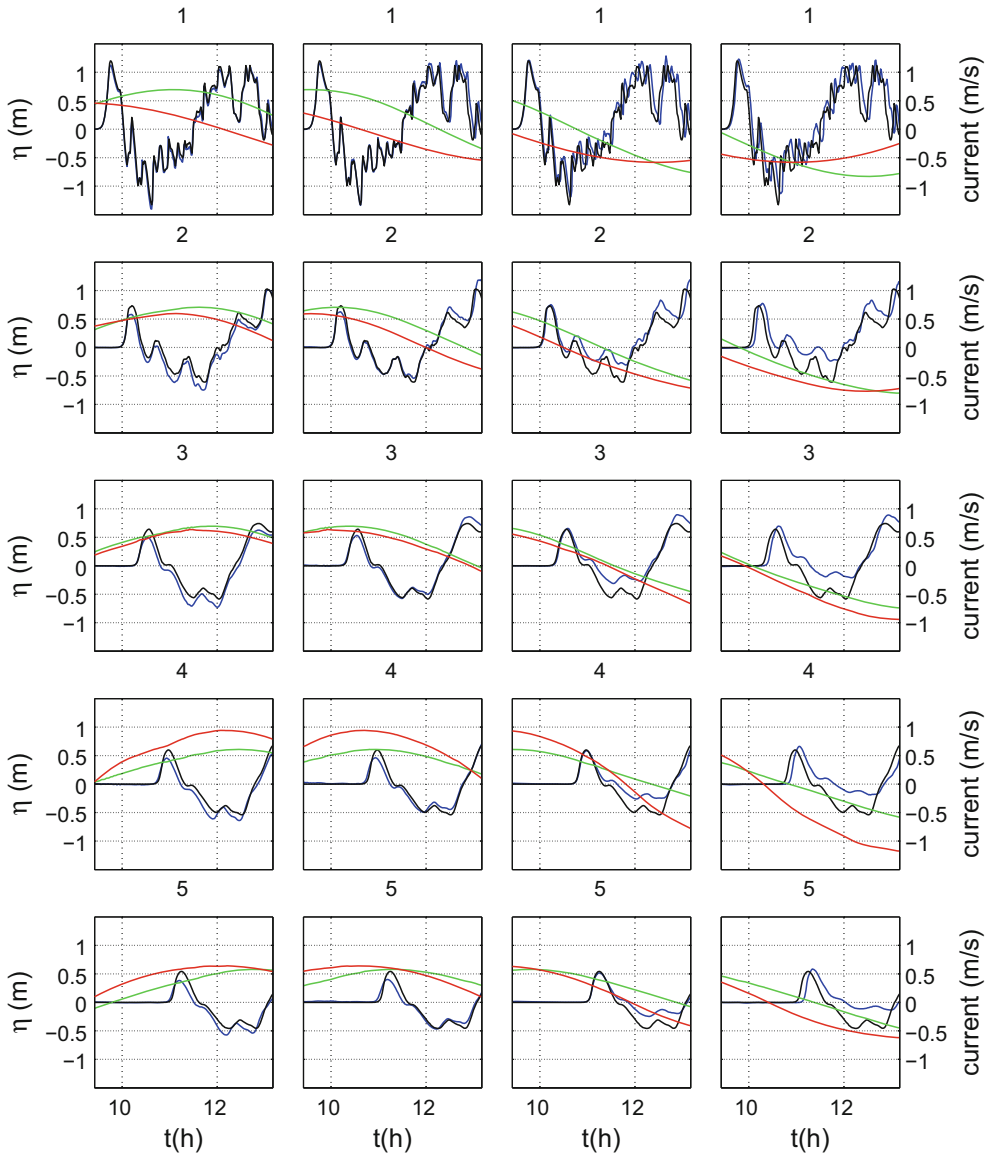

Figure 28
Same results as in Fig. 27 for the CVV tsunami

progressively increases as the tsunamis propagate up the HRE (from station #1 to 5).

In Figs. 27, 28 and 29, the patterns of surface elevations are similarly divided between the same stations, with at stations #2 to #5, most of the higher frequency oscillations having been filtered out. As could be expected from elementary long wave theory, when facing an opposite (ebbing) current tsunami elevations increase as compared to the simulations performed over a static MHW level, and they decrease when traveling with the (flooding) current. This becomes more prominent as the tsunamis propagate upstream the HRE. However, as this dynamic increase in surface elevation mostly occurs in the tail of the tsunami trains, while the tidal elevations are decreasing, this does not affect maximum flooding. When facing a co-flowing (flooding) tidal current, tsunami elevations, as for the currents, are

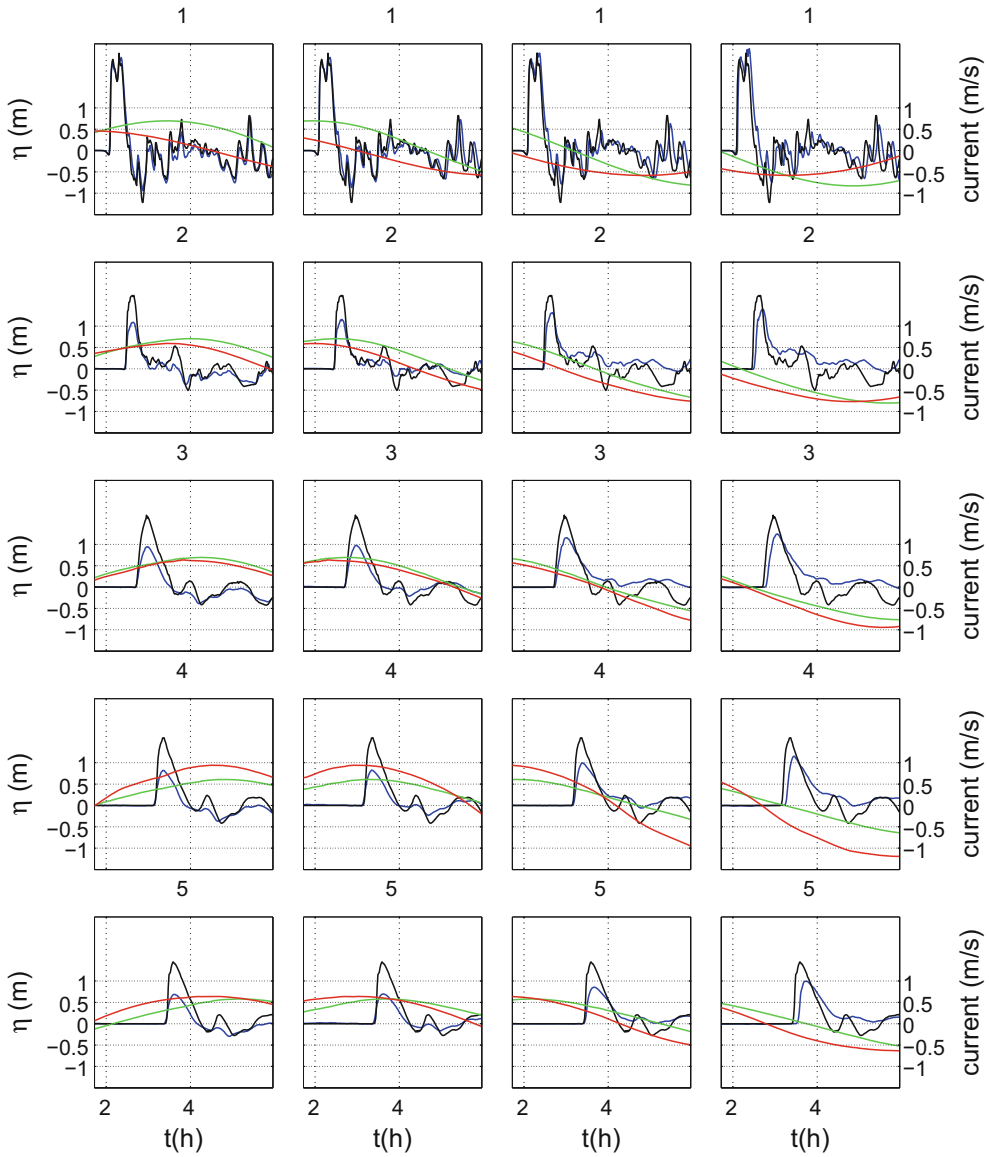

Figure 29
Same results as in Fig. 27 for the CRT SMF proxy tsunami

equal or slightly smaller than those found over a static MHW level. Consistent with observations made for the currents, changes in tsunami phase speed are observed, with the dynamic cases slightly lagging behind the static cases when facing an opposite (ebbing) tide current, and vice versa.

Overall, observed differences between dynamic and static tsunami–tide simulations are consistent with predictions of elementary wave theory on wave-current interactions. In grid G1, tidal currents exceed 1 m/s (2 kts), which is comparable to currents caused by the incoming PMTs. This similarity in current magnitude results in meaningful nonlinear interactions between the two long wave trains. At the entrance to Lower Bay (station #1 in Fig. 17), slack tide occurs about 1 h after high tide, but in the

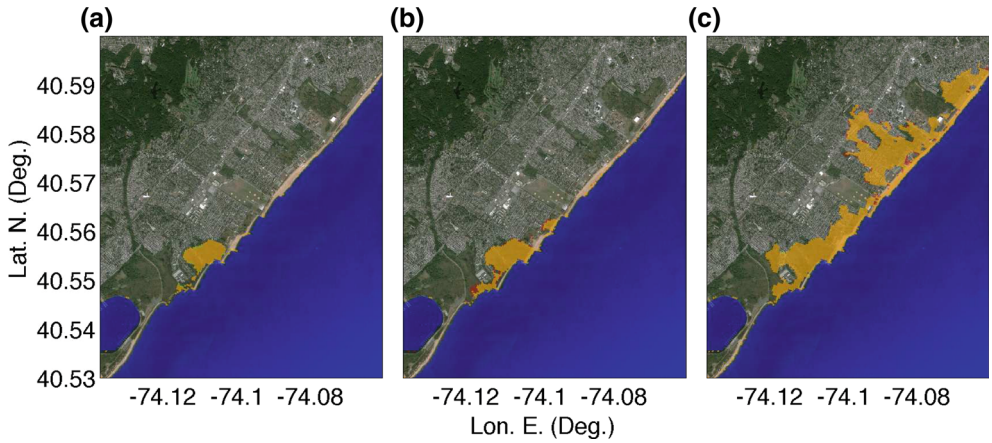

Figure 30
Extent of maximum tsunami inundation in eastern Staten Island from: (*yellow*) maximum envelopes computed over four tidal phases in dynamic tsunami–tide simulations (Fig. 22); and (*red*) the linear superposition of tsunamis over a static tide level (local MHW), for the three considered PMTs: **a** PRT, **b** CVV, and **c** CRT SMF proxy

Hudson River, flooding currents persist for more than two hours after high tide. Hence, leading tsunami crests arriving 1.5 h after high tide (during the initiation of the ebbing current) will still experience a favorable current in the Hudson River and thus will tend to decrease in elevation.

Another phenomenon affecting dynamic tsunami–tide simulations is that during lower tide elevation periods, the tsunamis propagate over shallower water areas and hence could end up shoaling somewhat more in some areas than in the static simulations; however, as results of the propagation over a lower tide have shown (i.e., 3 h delay), this in general does not lead to increased maximum flooding in the HRE over the entire simulation. Differences between surface elevation time series for the dynamic tsunami–tide simulations and those for the tsunami propagating over a static MHW level thus mostly result from nonlinear interactions between tide and tsunami currents.

7. Conclusions

We performed simulations of dynamic tsunami–tide interactions in the Hudson River estuary (HRE) and compared results to the standard tsunami simulations, which are performed over a static MHW tide level. In both cases, the maximum tide level (static or maximum dynamic) was selected as the average maximum tidal elevation reached in the HRE for an MHW tide during the period spanning 7:00 am on 13 July 2015 to 7:00 pm on 14 July 2015.

Overall, dynamic tsunami–tide simulations only predict a modest increase in maximum inundation in the HRE, 0.05–0.15 m for the three selected PMTs and four tide phases, as compared to static simulations. More specifically, Figs. 18, 19 and 21, which show maximum envelopes of differences between the dynamic and static results computed for each PMT and the three main tide phases considered here, and Fig. 23, which shows the envelopes of these, indicate that areas with the largest increases in surface elevation resulting from nonlinear tsunami–tide interactions are located at both the entrance and the southern region of Lower Bay (Sandy Hook Bay and Raritan Bay). Tsunamis arriving at the entrance to Lower Bay are trains of long waves that have nearly depth-uniform currents with maximum magnitude similar to that of currents caused by the selected tide. Results show that, for opposite currents, the three considered PMTs experience dynamic increases in surface elevations near high tide as far inland as Upper Bay (New York Harbor). Further upstream, the increase in bottom friction resulting from tsunami–tide interactions leads to reduced surface elevations as compared to a simulation over a static MHW level.

Although the maximum increases in surface elevation resulting from dynamic tsunami–tide interactions are both localized and not very significant in view of the maximum absolute tsunami flooding in the HRE (up to 3.5 m; Fig. 22), they nevertheless indicate that nonlinear interactions between tide and tsunami currents are meaningful. Hence, such interactions could become a significant factor in tsunami hazard assessment (such as performed in the NTHMP work), in bays or estuaries with larger tidal currents than in the HRE. Since dynamic tsunami–tide effects are highly site specific; however, when one suspects that significant tidal currents can occur, high-resolution simulations should be performed to accurately estimate their effects on local tsunami hazard, particularly if the coastline geometry and bottom topography are complex.

As a final illustration of this work, Fig. 30 shows the extent of maximum tsunami inundation on Staten Island predicted for the three PMTs (in each case, the envelope of the maximum elevation for the four considered tide phases), in the static and dynamic simulation cases. Staten Island is on the west side of Lower Bay, which is an area especially vulnerable to tsunami inundation. We see that the inundation extent of the dynamic case encompasses that of the static case, except in a very small area for the CVV case.

Acknowledgments

The authors gratefully acknowledge funding for this work, provided by Grants #NA14NWS4670041 and #NA15NWS4670029 of the U.S. National Tsunami Hazards Mitigation Program (NTHMP).

References

Abadie S, Harris JC, Grilli ST, Fabre R (2012) Numerical modeling of tsunami waves generated by the flank collapse of the Cumbre Vieja Volcano (La Palma, Canary Islands): Tsunami source and near-field effects. J Geophys Res *117*(CH03050), doi:10.1029/2011JC007646

Barkan R, ten Brink US, Lin J (2009) Far field tsunami simulations of the 1755 Lisbon earthquake: Implication for tsunami hazard to the U.S. East Coast and the Caribbean. Marine Geology *264*(1–2):109–122, doi:10.1016/j.margeo.2008.10.010

Dean RG, Dalrymple RA (1991) Water wave mechanics for engineers and scientists, Advanced Series on Ocean Engineering, vol 4. Prentice-Hall

FEMA (2014) Region II Storm Surge Project - Coastal Terrain Processing Methodology. Federal Emergency Management Agency (FEMA), Department of Homeland Security, 500 C Street, SW Washington DC, 20472

Geist E, Lynett P, Chaytor J (2009) Hydrodynamic modeling of tsunamis from the Currituck landslide. Marine Geology *264*:41–52, doi:10.1016/j.margeo.2008.09.005

Gica E, Spillane MC, Titov VV, Chamberlin CD, Newman J (2008) Development of the forecast propagation database for NOAA's short-term inundation forecast for tsunamis. NOAA tech. memo., National Oceanographic and Atmospheric Administration, OAR PMEL-139

Grilli AR, Grilli ST (2013a) Modeling of tsunami generation, propagation and regional impact along the U.S. East Coast from the Azores Convergence Zone. URL http://personal.egr.uri.edu/grilli//grilli-grilli-cacr-13-04, research Report no. CACR-13-04, 20 pps

Grilli AR, Grilli ST (2013b) Modeling of tsunami generation, propagation and regional impact along the upper U.S East Coast from the Puerto Rico trench. URL http://personal.egr.uri.edu/grilli//grilli-grilli-cacr-13-02

Grilli ST, Ioualalen M, Asavanant J, Shi F, Kirby JT, Watts P (2007) Source constraints and model simulation of the December 26, 2004 Indian Ocean tsunami. Journal of Waterway, Port, Coastal, and Ocean Engineering *133*(6):414–428, doi:10.1061/(ASCE0733-950X)2007133:6(414)

Grilli ST, Taylor ODS, Baxter CDP, Maretzki S (2009) Probabilistic approach for determining submarine landslide tsunami hazard along the upper East Coast of the United States. Marine Geology *264*(1–2):74–97, doi:10.1016/j.margeo.2009.02.010

Grilli ST, Dubosq S, Pophet N, Pérignon Y, Kirby JT, Shi F (2010) Numerical simulation and first-order hazard analysis of large co-seismic tsunamis generated in the Puerto Rico trench: near-field impact on the north shore of Puerto Rico and far-field impact on the US East Coast. Natural Hazards and Earth System Sciences *10*:2109–2125, doi:10.5194/nhess-2109-2010

Grilli ST, Harris JC, Tajalli-Bakhsh TS, Masterlark TL, Kyriakopoulos C, Kirby JT, Shi F (2013) Numerical simulation of the 2011 Tohoku tsunami based on a new transient FEM co-seismic source: Comparison to far- and near-field observations. Pure and Applied Geophysics 170:1333–1359, doi:10.1007/s00024-012-0528-y

Grilli ST, Grilli AR, Tehranirad B, Kirby JT (2015a) Modeling tsunami sources and their propagation in the Atlantic Ocean for coastal tsunami hazard assessment and inundation mapping along the US East Coast. In: Proc. 2015 COPRI Solutions to Coastal Disasters Conf. (Boston, USA. September 9-11, 2015, American Soc. Civil Eng., p 12. URL http://personal.egr.uri.edu/grilli/COPRI15_sgrilli.pdf

Grilli ST, O'Reilly C, Harris JC, Tajalli-Bakhsh T, Tehranirad B, Banihashemi S, Kirby JT, Baxter CD, Eggeling T, Ma G, Shi F (2015b) Modeling of SMF tsunami hazard along the upper US East Coast: Detailed impact around Ocean City, MD. Natural Hazards *76*(2):705–746, doi:10.1007/s11069-014-1522-8

Ioualalen M, Asavanant J, Kaewbanjak N, Grilli ST, Kirby JT, Watts P (2007) Modeling the 26th December 2004 Indian Ocean tsunami: Case study of impact in Thailand. J Geophys Res 112:C07,024, doi:10.1029/2006JC003850

Kirby JT, Shi F, Tehranirad B, Harris JC, Grilli ST (2013) Dispersive tsunami waves in the ocean: Model equations and sensitivity to dispersion and Coriolis effects. Ocean Modelling *62*:39–55, doi:10.1016/j.ocemod.2012.11.009

Kowalik Z, Proshutinsky A (2010) Tsunami-tide interactions: A Cook Inlet case study. Continental Shelf Research *30*(6):633–642, doi:10.1016/j.csr.2009.10.004

Kowalik Z, Proshutinsky T, Proshutinsky A (2006) Tide–tsunami interactions. Science of Tsunami Hazards *24*(4):242–256

Ma G, Shi F, Kirby JT (2012) Shock-capturing non-hydrostatic model for fully dispersive surface wave processes. Ocean Modelling *43–44*:22–35, doi:10.1016/j.ocemod.2011.12.002

Nakada S, Hayashi M, Koshimura S, Yoneda S, Kobayashi E (2015) Tsunami simulation generated by the greatest earthquake scenario along the Nankai Trough under consideration of tidal currents in a large bay. In: Proc. 25th Intl Ocean and Polar Engng Conf (iSOPE25, Hawaii, HI, June 2015), International Society of Offshore and Polar Engineers, pp 811–816

NOAA-NGDC (2013) National geophysical data center, U.S. coastal relief mode. URL http://www.ngdc.noaa.gov/mgg/coastal/crm.html, retrieved December 2013

Okada Y (1985) Surface deformation due to shear and tensile faults in a half space. Bull Seismol Soc America *75*(4):1135–1154

Shi F, Kirby JT, Harris JC, Geiman JD, Grilli ST (2012) A high-order adaptive time-stepping TVD solver for Boussinesq modeling of breaking waves and coastal inundation. Ocean Modelling *43–44*:36–51, doi:10.1016/j.ocemod.2011.12.004

Shi F, Kirby JT, Tehranirad B (2012b) Tsunami benchmark results for spherical coordinate version of FUNWAVE-TVD (version 1.1). Tech. rep., Center for Applied Coastal Research, Univ. of Delaware, research Report no. CACR-12-02

Stammer D, Ray RD, Andersen OB, Arbic BK, Bosch W, Carrere L, Cheng Y, Chinn DS, Dushaw BD, Egbert GD, Erofeeva SY, Fok HS, Green JAM, Griffiths S, King MA, Lapin V, Lemoine FG, Luthcke SB, Lyard F, Morison J, Muller M, Padman L, Richman JG, Shriver JF, Shum CK, Taguchi E, Yi T (2014) Accuracy assessment of global barotropic ocean tide models. Reviews of Geophysics *52*(3):243–282, doi:10.1002/2014RG000450

Tajalli-Bakhsh TS, Grilli ST, Grilli AR (2014) Dynamic tide effects on tsunami coastal hazard in large estuaries: Case of the Chesapeake Bay/James River, USA. Tech. rep., Center for Applied Coastal Research, Dept. of Civil and Environmental Engineering, University of Delaware, URL http://personal.egr.uri.edu/grilli//Tajelli-etal-cacr-15-09.pdf, research Report no. CACR-15-09, 42 pps

Tehranirad B, Shi F, Kirby JT, Harris JC, Grilli ST (2011) Tsunami benchmark results for fully nonlinear Boussinesq wave model FUNWAVE-TVD, version 1.0. Tech. rep., Center for Applied Coastal Research, University of Delaware, research Report No. CACR-11-02

Tehranirad B, Banihashemi S, Kirby JT, Callahan JA, Shi F (2014) Tsunami inundation mapping for Ocean City, MD NGDC DEM. Tech. rep., Center for Applied Coastal Research, Department of Civil and Environmental Engineering, University of Delaware, research Report No. CACR-14-04

Tehranirad B, Harris JC, Grilli AR, Grilli ST, Abadie S, Kirby JT, Shi F (2015) Far-field tsunami hazard in the North Atlantic basin from large scale flank collapses of the Cumbre Vieja Volcano, La Palma. Pure Appl Geophys 172(12):3589–3616. doi:10.1007/s00024-015-1135-5

ten Brink US, Twichell D, Geist E, Chaytor JD, Locat J, Lee H, Buczkowski B, Barkan R, Solow A, Andrews BD, Parsons T, Lynett P, Lin J, Sansoucy M (2008) Evaluation of tsunami sources with the potential to impact the U.S. Atlantic and Gulf Coasts. Tech. rep., USGS Administrative report to the U.S. Nuclear Regulatory Commission, 300 pps

ten Brink US, Chaytor JD, Geist EL, Brothers DS, Andrews BD (2014) Assessment of tsunami hazard to the US Atlantic margin. Marine Geology *353*:31–54, doi:10.1016/j.margeo.2014.02.011

Tolkova E (2013) Tide-tsunami interaction in the Columbia River, as implied by historical data and numerical simulations. Pure and Applied Geophysics *170*(6–8):1115–1126, doi:10.1007/s00024-012-0518-0

Tolkova E, Tanaka H, Roh M (2015) Tsunami observations in rivers from a perspective of tsunami interaction with tide and riverine flow. Pure and Applied Geophysics *172*(3–4):953–968, doi:10.1007/s00024-014-1017-2

USGS (2010) Estimates of monthly and annual net discharge, in cubic feet per second, of Hudson River at New York, N.Y. (mouth). URL http://ny.water.usgs.gov/projects/dialer_plots/Hudson_R_at_NYC_Freshwater_Discharge.htm, U.S. Department of the Interior, US Geological Survey

Ward SN, Day S (2001) Cumbre Vieja Volcano potential collapse at La Palma, Canary Islands. Geophysical Research Letter *28*(17):3397–3400, doi:10.1029/2001GL013110

Wei G, Kirby JT, Grilli ST, Subramanya R (1995) A fully nonlinear Boussinesq model for free surface waves. part i: Highly nonlinear unsteady waves. Journal of Fluid Mechanics *294*:71–92

Yeh H, Tolkova E, Jay D, Talke S, Fritz H (2012) Tsunami hydrodynamics in the Columbia River. J Disaster Res *7*(5):604–608. doi:10.1007/s00024-012-0489-1

Zhang YL, Witter RC, Priest GR (2011) Tsunami–tide interaction in 1964 Prince Williams Sound tsunami. Ocean Modelling *40*(3–4):246–259. doi:10.1016/j.ocemod.2011.09.005

(Received November 23, 2015, revised April 29, 2016, accepted May 4, 2016, Published online May 24, 2016)